bioRxiv preprint doi: https://doi.org/10.1101/2023.02.27.530319; this version posted February 28, 2023. The copyright holder for this preprint (which was not certified by peer review) is the author/funder, who has granted bioRxiv a license to display the preprint in perpetuity. It is made available under aCC-BY 4.0 International license.

A Conserved Requirement for RME-8/DNAJC13 in Neuronal Autolysosome Reformation

Sierra Swords[1], Nuo Jia[2], Anne Norris[1], Jil Modi[1], Qian Cai[2], and Barth D. Grant[1,3]

[1] Department of Molecular Biology and Biochemistry Rutgers University, Piscataway, NJ USA, 08854

[2] Department of Cell Biology and Neuroscience, Rutgers University, Piscataway, NJ USA, 08854

[3] Center for Lipid Research, New Brunswick, NJ USA 08901

Corresponding Author: Barth D. Grant

Email address: barthgra@dls.rutgers.edu

Tel: 848-445-7339

bioRxiv preprint doi: https://doi.org/10.1101/2023.02.27.530319; this version posted February 28, 2023. The copyright holder for this preprint (which was not certified by peer review) is the author/funder, who has granted bioRxiv a license to display the preprint in perpetuity. It is made available under aCC-BY 4.0 International license.

ABSTRACT

Autophagosomes fuse with lysosomes, forming autolysosomes that degrade engulfed cargo. To maintain lysosomal capacity, autolysosome reformation (ALR) must regenerate lysosomes from autolysosomes using a membrane tubule-based process. Maintaining lysosomal capacity is required to maintain proteostasis and cellular health, especially in neurons where lysosomal dysfunction has been repeatedly implicated in neurodegenerative disease. Cell biological studies have linked the DNA-J domain Hsc70 co-chaperone RME-8/DNAJC13 to endosomal coat protein regulation, while human genetics studies have linked RME-8/DNAJC13 to neurological disease, including Parkinsonism and Essential Tremor. We report new analysis of the requirements for the RME-8/DNAJC13 protein in neurons, focusing on *C. elegans* mechanosensory neurons in the intact animal, and in primary mouse cortical neurons in culture. We find that loss of RME-8/DNAJC13 in both systems results in accumulation of grossly elongated autolysosomal tubules. Further *C. elegans* analysis revealed a similar autolysosome tubule accumulation defect in mutants known to be required for ALR in mammals, including *bec-1/beclin* and *vps-15/PIK3R4/p150* that regulate type-III PI3-kinase VPS-34, and *dyn-1*/dynamin that severs ALR tubules. Clathrin is also an important ALR regulator implicated in autolysosome tubule formation and release. In *C. elegans* we found that loss of RME-8 causes severe depletion of clathrin from neuronal autolysosomes, a phenotype shared with *bec-1* and *vps-15* mutants. We conclude that RME-8/DNAJC13 plays a conserved but previously unrecognized role in autolysosome reformation, likely affecting ALR tubule initiation and/or severing. Additionally, in both systems, we found that loss of RME-8/DNAJC13 appeared to reduce autophagic flux, suggesting feedback regulation from ALR to autophagy. Our results

bioRxiv preprint doi: https://doi.org/10.1101/2023.02.27.530319; this version posted February 28, 2023. The copyright holder for this preprint (which was not certified by peer review) is the author/funder, who has granted bioRxiv a license to display the preprint in perpetuity. It is made available under aCC-BY 4.0 International license.

connecting RME-8/DNAJC13 to ALR and autophagy provide a potential mechanism by which RME-8/DNAJC13 could influence neuronal health and the progression of neurodegenerative disease.

INTRODUCTION

Organelle integrity and cellular proteostasis depend heavily upon a variety of degradative mechanisms for macromolecular turnover. Among these, one key pathway is macroautophagy (hereafter referred to as autophagy), a mechanism that can remove whole defective organelles and cytoplasmic protein aggregates as they build up, ameliorating the cellular dysfunction that can occur if such components accumulate. Autophagy begins with the phagophore, a *de novo* membrane which expands to completely engulf a region of cytoplasm, often including a specific degradative target, forming a double-membraned autophagosome. Once autophagosomes form, they fuse with lysosomes, creating autolysosomes to degrade their contents.

Lysosomes are reformed from autolysosomes using a specific mechanism, termed autolysosome reformation (ALR)[1]. This autolysosome reformation (ALR) process is required to maintain the active lysosome pool, allowing degradation of autophagic contents to continue uninterrupted[1]. During ALR, recycling tubules are drawn out from buds on the autolysosome limiting membrane and are then severed to release protolysosomes. The mechanism of ALR tubule formation and release is not well understood, but appears to require phosphoinositide lipids PI(3)P and PI(4,5)P_2, a clathrin coat, the severing enzyme dynamin, and kinesin motor

bioRxiv preprint doi: https://doi.org/10.1101/2023.02.27.530319; this version posted February 28, 2023. The copyright holder for this preprint (which was not certified by peer review) is the author/funder, who has granted bioRxiv a license to display the preprint in perpetuity. It is made available under aCC-BY 4.0 International license.

activity[2-5]. ALR failure is typically characterized by the accumulation of enlarged autolysosomes and grossly elongated autolysosomal tubules [2, 6]. Interestingly, in some cases ALR defects have been linked to impaired autophagy, suggesting feedback from ALR to autophagy initiation[5].

Autophagy is thought to be particularly important in neurons, with neurons displaying higher levels of constitutive autophagy compared to other cell types[7, 8]. This higher level of basal autophagy implies a necessary requirement for higher level basal ALR to maintain lysosomal capacity. Neurodegenerative diseases such as Alzheimer's and Parkinson's Disease (PD) are strongly linked with impaired degradation in general, especially decreased autophagy that is thought to contribute to a build-up of deleterious protein aggregates, such as tau, amyloid beta, and α-synuclein, especially as aging occurs (reviewed in [9, 10]). Since most neurons are post-mitotic, they are unable to dilute out protein aggregates via mitosis, an option available for non-terminally differentiated cell types. Neurons also have extremely long, thin axons that proteins and cargoes need to traverse. This architecture makes neurons especially sensitive to neurodegeneration should autophagy and other aggregate clearance mechanisms go awry. This likely includes ALR, as in several cases failure in ALR has been linked to neurodegenerative diseases [11, 12].

We became interested in the potential role of RME-8 in neuronal health when a Parkinson's Disease-linked variant of human RME-8/DNAJC13 was identified in a multi-incident Mennonite family [13]. The PD-linked mutation, N855S, alters a residue that is absolutely conserved within

bioRxiv preprint doi: https://doi.org/10.1101/2023.02.27.530319; this version posted February 28, 2023. The copyright holder for this preprint (which was not certified by peer review) is the author/funder, who has granted bioRxiv a license to display the preprint in perpetuity. It is made available under aCC-BY 4.0 International license.

88 organisms that possess a nervous system [14, 15]. Patients with this allele displayed late onset
89 PD with α-synuclein-positive Lewy Body pathology[13, 16]. Other alleles of RME-8/DNAJC13
90 have also been implicated in PD pathogenesis, and RME-8/DNAJC13 variants have been
91 reported as associated with other neurological disorders, including familial Essential Tremor
92 and Tourette's Syndrome [17]. Association of RME-8/DNAJC13 with multiple neurologic
93 diseases and syndromes highlights a crucial and unexplored role for RME-8 in neuronal health.
94
95 RME-8 is a widely conserved DNAJ-domain Hsc70 co-chaperone that we first discovered in our
96 *C. elegans* screens for endosomal regulators[15, 18-20]. RME-8 contains at least one N-terminal
97 PI(3)P lipid binding domain prior to the central J-domain that recruits RME-8 to endosomes [15,
98 21]. On sorting endosomes, RME-8 and its binding partner SNX-1/Snx1 localize to a
99 microdomain functioning in cargo recycling, adjacent a microdomain functioning in cargo
100 degradation on the same endosome[15, 22-24]. The degradative domain is marked by the
101 ESCRT complex component HRS and a flat clathrin lattice[25-27]. In the absence of RME-8 and
102 its binding partner SNX-1/Snx1, both HRS and clathrin overaccumulate on endosomal
103 membranes, causing dysfunction of cargo sorting within endosomes [24, 28]. Sorting
104 endosomes mature into late endosomes. Like autophagosomes, late endosomes must fuse with
105 lysosomes to degrade their contents.
106
107 Here we investigated the requirements for RME-8 in *C. elegans* mechanosensory neurons in the
108 intact animal, and in primary mouse cortical neurons in culture. Depletion of RME-8/DNAJC13
109 caused neurons in both systems to accumulate LMP-1/LAMP1 and LGG-1/LC3 positive

bioRxiv preprint doi: https://doi.org/10.1101/2023.02.27.530319; this version posted February 28, 2023. The copyright holder for this preprint (which was not certified by peer review) is the author/funder, who has granted bioRxiv a license to display the preprint in perpetuity. It is made available under aCC-BY 4.0 International license.

autolysosomes bearing grossly elongated membrane tubules. In mouse cortical neurons, we also found that depletion of RME-8/DNAJC13 resulted in gross enlargement of the autolysosomes, and loss of most LC3-negative lysosomes. Further *C. elegans* analysis revealed a similar autolysosome tubule accumulation defect in mutants known to be required for ALR in mammals, including *bec-1/beclin* and *vps-15/PIK3R4/p150* that regulate the VPS-34 type-III PI3-kinase, and *dyn-1/dynamin* that severs ALR tubules. Furthermore, we found that loss of RME-8 causes severe depletion of clathrin from autolysosomes, a phenotype also shared with *snx-1*, *bec-1* and *vps-15* mutants. Taken together, we conclude that RME-8/DNAJC13 plays a conserved but previously unrecognized role in autolysosome reformation, likely affecting ALR tubule severing. Additionally, in both systems, we found that loss of RME-8/DNAJC13 reduced autophagic flux, suggesting feedback regulation from ALR to autophagy. These results connecting RME-8/DNAJC13 to ALR and autophagy provide a potential mechanism by which RME-8/DNAJC13 could influence neuronal health and the progression of neurodegenerative diseases, including Parkinson's Disease.

RESULTS

Loss of RME-8 function results in accumulation of long lysosomal tubules

Given the association of RME-8/DNAJC13 with neurological disease[13, 17, 29-32], we sought to better understand RME-8 function in neurons of *C. elegans* where RME-8-mediated trafficking mechanisms were first elucidated[15, 19, 23, 24]). Here we focused on the mechanosensory

bioRxiv preprint doi: https://doi.org/10.1101/2023.02.27.530319; this version posted February 28, 2023. The copyright holder for this preprint (which was not certified by peer review) is the author/funder, who has granted bioRxiv a license to display the preprint in perpetuity. It is made available under aCC-BY 4.0 International license.

touch neurons, in particular analyzing the two centrally located touch neurons referred to as ALM right and ALM left (Figure 1A). All six touch neurons are embedded in the hypodermis (skin), very close to the cuticle, where they sense gentle mechanical stimuli[33]. The stereotyped location of the ALM neurons close to the exterior of the animal, and their simple architecture with one main process that extends anteriorly to make synapses in the head, make these neurons ideal for quantitative imaging in the living, intact animal. To allow subcellular analysis specifically in these neurons, we expressed a variety of fluorescently tagged proteins from single copy transgenes, driven by the mechanosensory touch neuron-specific *mec-7* promoter[34].

rme-8 is an essential gene, so for most experiments we measured the effects of loss of RME-8 function on neuronal trafficking using the well-characterized temperature sensitive allele, *rme-8*(*b1023ts)*[19]. Temperature shifting this strain from the permissive temperature (15°C) to the non-permissive temperature (25°C) is known to destabilize the RME-8 protein, and results in clear phenotypes within 24 hours[19]. For most experiments we temperature shifted *rme-8*(*b1023ts)* animals at the L4 stage, and conducted imaging experiments in young adults 24-30 hours later. For some experiments we also analyzed the effects of *rme-8(pw22[N861S])*, an allele we generated by CRISPR-based genome engineering to mimic the human late onset Parkinson's associated allele N855S[13]. *rme-8(pw22[N861S])* bears an equivalent point mutation to N855S, changing asparagine 861 to serine (N861S).

bioRxiv preprint doi: https://doi.org/10.1101/2023.02.27.530319; this version posted February 28, 2023. The copyright holder for this preprint (which was not certified by peer review) is the author/funder, who has granted bioRxiv a license to display the preprint in perpetuity. It is made available under aCC-BY 4.0 International license.

Given the known roles of RME-8 on endosomes, and the association of neurodegenerative disease with membrane trafficking pathway dysfunction, we initially analyzed the effects of the *rme-8(ts)* mutant on late endosomes and lysosomes using an mScarlet::RAB-7 marker expressed in the mechanosensory neurons. Importantly, in young adult (adult Day 1) *rme-8(b1023ts)* mutants we noted the appearance of RAB-7 vesicles bearing highly elongated tubules, a morphology not observed in control animals (Figure 1B, white arrowhead; quantified in 1C). We also assayed for this phenotype in the PD-allele mimic *rme-8(N861S)*. Interestingly, we observed a similar accumulation of elongated RAB-7-positive tubules in aged animals in late adulthood (adult Day 9), but not in young adults (Figure 1D-E). This mimics the late-onset nature of the homologous PD-linked allele in human patients, suggesting that the N861S allele confers a similar but more subtle defect than the *b1023ts* loss of function allele. Tubules emanating from endosomes and lysosomes are generally associated with recycling processes, with accumulation of exaggerated tubules often associated with defects in tubule release.

To better define the nature of these vesicles, we extended our analysis using LMP-1/LAMP1 fused to mNeonGreen (mNG), a transmembrane marker of lysosomes (Figure 1F). We noted a very similar phenotype using the lysosome marker in *rme-8(b1023ts)* mutants, measuring a highly significant increase in LMP-1 tubule length (Figure 1G). We noted that in many cases these long thin tubules appeared connected to a larger vesicle located in the neuronal soma (white arrow, Figure 1F; Video S1), and in others the vesicle and tubule were located in the soma-proximal neuronal process (white arrowhead, Figure 1F). These persistent tubules were not seen in *rme-8(+)* backgrounds (Figure 1F, Video S2). We extended this analysis, measuring

bioRxiv preprint doi: https://doi.org/10.1101/2023.02.27.530319; this version posted February 28, 2023. The copyright holder for this preprint (which was not certified by peer review) is the author/funder, who has granted bioRxiv a license to display the preprint in perpetuity. It is made available under aCC-BY 4.0 International license.

174 the intensity LMP-1::mNG labeling of lysosomes in the soma, dendrite, and proximal axon.
175 Interestingly, LMP-1 integrated intensity was increased upon loss of RME-8, indicating a
176 significant abnormal accumulation of LMP-1 labeled lysosomes within neurons upon loss of
177 RME-8 (Figure 1H). These data indicate a key requirement for RME-8 in neuronal lysosome
178 homeostasis.
179
180 RME-8 function is touch neuron autonomous
181 To confirm that the lysosomal tubule phenotype is caused by loss of RME-8, and test if RME-8 is
182 required autonomously within the touch neurons to maintain lysosome homeostasis, we tested
183 for rescue of the neuronal *rme-8(b1023ts)* phenotype in animals expressing a touch neuron-
184 specific *rme-8(+)* minigene. Indeed, we observed that expressing wild-type RME-8 in just the six
185 touch neurons rescued touch neuron lysosomal tubule accumulation (Figure 1I-J).
186
187 RME-8 affects autolysosomes
188 Lysosomes receive cargo via membrane fusion, fusing with endosomes, phagosomes, and
189 autophagosomes to form endolysosomes, phagolysosomes, and autolysosomes respectively
190 (reviewed in [35-37]). Neurons in particular display high levels of basal autophagy compared to
191 other cell types[8]. Thus, we sought to determine to what extent the LMP-1 positive structures
192 we observed in the touch neurons represent autolysosomes. To achieve this, we created strains
193 expressing the autophagosome marker mNG::LGG-1 and LMP-1::mScarlet-I (mSc) in touch
194 neurons (Figure 2A). We measured a 75% pixel overlap of mNG::LGG-1 and LMP-1::mSc, with
195 virtually all LMP-1-positive lysosomes containing at least some mNG::LGG-1, indicating that

bioRxiv preprint doi: https://doi.org/10.1101/2023.02.27.530319; this version posted February 28, 2023. The copyright holder for this preprint (which was not certified by peer review) is the author/funder, who has granted bioRxiv a license to display the preprint in perpetuity. It is made available under aCC-BY 4.0 International license.

196 they are autolysosomes (Figure 2B). We only rarely observed mNG::LGG-1 labeled objects
197 lacking LMP-1::mSc (Figure 2A, white arrow), indicating that at steady state most
198 autophagosomes have already fused with lysosomes.
199
200 We observed the grossly elongated tubules (white arrowhead) in *rme-8(b1023ts)* mutants in
201 LMP-1::mSc; mNG::LGG-1 double labeled strains (Figure 2A) and in single labeled mNG::LGG-1
202 strains (Figure 2C, quantified in 2D). We noted that the overall mNG::LGG-1 signal was weaker
203 in *rme-8* mutants, with mNG::LGG-1 fluorescence particularly weak and difficult to detect in the
204 tubules. mNG::LGG-1 fluorescence was much more prominent in vesicular region of the
205 neuronal autolysosomes (observed in Figures 2A, 2C). This was reflected in a maintained 76%
206 overlap of LGG-1-positive area that colocalized with LMP-1 in *rme-8(b1023ts)* mutants, but a
207 reduced percentage of LMP-1-positive area that colocalized with LGG-1 signal in *rme-*
208 *8(b1023ts)* mutants (Figure 2B). We also measured a reduced overall integrated intensity for
209 LGG-1::mNG puncta in the neuronal soma in *rme-8(b1023ts)* mutants (Figure 2E). Taken
210 together our results indicate that *C. elegans* touch neurons maintain active autophagy under
211 well-fed conditions, and most lysosomes in the neuronal soma have previously fused with
212 autophagosomes, with loss of RME-8 leading to accumulation of abnormal autolysosome-
213 derived membrane tubules.
214
215 <u>Loss of RME-8 phenocopies autolysosome reformation mutants</u>
216 The strikingly elongated LMP-1-positive tubules emanating from autolysosome puncta were
217 highly reminiscent of autolysosome reformation tubules as reported in mammalian cells[1, 2, 4,

bioRxiv preprint doi: https://doi.org/10.1101/2023.02.27.530319; this version posted February 28, 2023. The copyright holder for this preprint (which was not certified by peer review) is the author/funder, who has granted bioRxiv a license to display the preprint in perpetuity. It is made available under aCC-BY 4.0 International license.

6, 38]. ALR tubules will persist and elongate if the mechanism by which the tubules are severed is impaired[2, 4, 6, 38, 39]. Our observations that LMP-1/LAMP1 intensity in the autolysosomes increased in *rme-8* mutants suggests a failure to recycle LMP-1 out of the autolysosome, further supporting the hypothesis that the elongated tubules accumulating in *rme-8* mutant neurons represent an accumulating ALR intermediate (Figure 2). Similar effects have been observed in other organisms when ALR was impaired[38].

If the *rme-8* mutant phenotype indicates a defect in neuronal ALR, we would expect to find similar phenotypes in *C. elegans* mutants lacking proteins previously identified as ALR regulators in other systems. In particular, enzymes that regulate lysosomal phosphatidylinositol 4,5-bisphosphate ($PI(4,5)P_2$), phosphatidylinositol 3-phosphate ($PI(3)P$), as well as the coat protein clathrin and the membrane severing GTPase dynamin, have been suggested to function in ALR, in addition to their more well-known roles in other trafficking steps [2, 3, 6]. For instance, mammalian cells inhibited for class III phosphoinositide 3-kinase VPS34 activity display lysosomal tubule accumulation during ALR [6]. To impair the VPS-34 complex in *C. elegans*, we used mutants in *bec-1/beclin* and *vps-15/PIK3R4/p150*, key regulators of VPS-34 activity[40-42]. We observed severely elongated LMP-1::mNG tubules in *bec-1* and *vps-15* mutants that strongly resemble those we found in *rme-8* mutants (Figure 3A, white arrowheads, quantified in 3B). We also examined the tubule accumulation phenotype in neurons impaired for dynamin[43]. Previous work showed that mammalian dynamin 2 binds to autolysosome tubules along their length, and pharmacologic inhibition of dynamin 2 in hepatocytes produced enlarged autolysosomes bearing extremely long, thin LAMP1-positive tubules[3]. Importantly, we also found that *dyn-1(ts)* mutants displayed dramatic tubulation of LMP-1-positive

bioRxiv preprint doi: https://doi.org/10.1101/2023.02.27.530319; this version posted February 28, 2023. The copyright holder for this preprint (which was not certified by peer review) is the author/funder, who has granted bioRxiv a license to display the preprint in perpetuity. It is made available under aCC-BY 4.0 International license.

autolysosomes in the *C. elegans* touch neurons (Figure 3B). Taken together our results indicate phylogenetic conservation of function in autolysosome tubule severing mechanisms from nematode to human and suggest that RME-8 is important for autolysosome tubule release.

Mammalian RME-8/DNAJC13 is also required for neuronal ALR

We also sought to determine if RME-8 (also called DNAJC13) is required for ALR in mammalian neurons. To test this, we analyzed primary cortical neurons derived from the embryonic mouse brain, visualizing autolysosomes with GFP-LAMP1 and mRFP-LC3, knocking down mouse RME-8/DNAJC13 using shRNAs. Importantly, in neurons expressing RME-8/DNAJC13 shRNA, we observed strikingly elongated LAMP1-labeled tubules emanating from vesicles positive for mRFP-LC3, identifying them as autolysosomes (Figure 4A). Under these conditions LAMP1-positive tubule length increased from a mean of <4 um in control shRNA neurons, to ~18 um in RME-8/DNAJC13 shRNA neurons (Figure 4B). Elongated LAMP1-positive tubules in RME-8/DNAJC13 knock down conditions can be seen in Video S3, and compared to the dynamics of lysosomes in neurons expressing control shRNA (Video S4). The proportion of long tubules was much greater upon knock down of RME-8/DNAJC13, with 39% of tubules having a length of greater than 20um upon loss of RME-8, while 0% of tubules in control cells were longer than 20um (Figure 4C). We also noted that the autolysosomes in RME-8/DNAJC13 knockdown neurons were greatly enlarged, in many cases displaying areas >3 times greater than in controls (Figure 4D), and were fewer in number (Figure4E). This is similar to previously described ALR defects upon loss of known ALR regulators, that also develop enlarged LAMP1-positive autolysosomes due to an inability to recycle material out of the lysosomes after fusion with

bioRxiv preprint doi: https://doi.org/10.1101/2023.02.27.530319; this version posted February 28, 2023. The copyright holder for this preprint (which was not certified by peer review) is the author/funder, who has granted bioRxiv a license to display the preprint in perpetuity. It is made available under aCC-BY 4.0 International license.

autophagosomes [1-4]. We also observed a significantly reduced number of LAMP1-positive lysosomes that lack LC3 in RME-8/DNAJC13 knockdown neurons (Figure 4F), further indicating a defect in lysosome reformation from autolysosomes. Taken together our results indicate a clear requirement for RME-8 in completion of ALR in *C. elegans* and mammalian neurons.

RME-8 localization in neurons

RME-8 in neurons could function in ALR directly via a role on autolysosomes, or it could affect ALR indirectly, for instance through endosomes which also fuse with lysosomes, potentially providing regulatory molecules in addition to degradative cargo. To assay RME-8 subcellular localization in *C. elegans* we expressed a rescuing touch-neuron-specific RME-8::GFP transgene. At steady state we did not observe a high degree of RME-8::GFP on LMP-1::mSc-positive lysosomes in the *C. elegans* touch neurons, but some overlap was detected (Figure 5A-B). We observed a high degree of colocalization of RME-8::GFP and endosome marker mSc::SNX-1 in the neuronal soma, similar to our previous results in other cell types (Figure 5A-B). In summary, if RME-8 functions directly on autolysosomes during ALR, it is likely to be transiently associated with a small region of the autolysosome, as has been proposed for proteins like dynamin that participate in autolysosome tubule fission[3].

Reduced neuronal autophagy in *C. elegans rme-8* mutants

Given the apparent reduced intensity of mNG::LGG-1 we observed in *rme-8* mutants, we asked if known ALR-relevant proteins are important for maintaining autophagic flux in *C. elegans* neurons. We first investigated this by comparing mNG::LGG-1 levels in touch neuron somata of *rme-8*, *bec-1*, *vps-15*, and *dyn-1* mutants (Figure 6A). Beyond ALR, VPS-15 and BEC-1 also impinge upon PI(3)P generation at the omegasome, a pre-autophagosomal structure, but

bioRxiv preprint doi: https://doi.org/10.1101/2023.02.27.530319; this version posted February 28, 2023. The copyright holder for this preprint (which was not certified by peer review) is the author/funder, who has granted bioRxiv a license to display the preprint in perpetuity. It is made available under aCC-BY 4.0 International license.

283 dynamin has not been linked to any direct role in autophagosome formation [44, 45]. We
284 observed a similar decrease in both the integrated and average intensity of mNG::LGG-1 puncta
285 in *rme-8*, *dyn-1/dynamin*, *bec-1/beclin*, and *vps-15* mutants (Figure 6B-C). These results are
286 consistent with recent studies linking impaired ALR to decreased autophagy initiation[38].
287 We also examined mNG::LGG-1 levels and distribution in *epg-1/atg13-like*[46], *epg-6/atg18-*
288 *like*[47], and *epg-8* mutants[48]. These proteins have clearly defined roles within the canonical
289 autophagic initiation pathway, but without known effects on ALR. We found that *epg-1*, *epg-6*,
290 and *epg-8* mutants displayed a strongly diffusive mNG::LGG-1 signal in the touch neuron soma,
291 with two or three apparent large aggregates near the nucleus (Figure 6D; white arrowheads).
292 While *epg-1*, *epg-6*, and *epg-8* all have decreased integrated intensities (Figure 6E), similar to
293 ALR mutants, the average intensity of the puncta is significantly higher than wild-type puncta
294 (Figure 6F), in stark contrast to the decreased average intensity of ALR mutants (Figure 6C). This
295 aggregation phenotype has been previously observed in cells expressing tagged LGG-1 in which
296 autophagy initiation is strongly blocked, as expected in these mutants, resulting in
297 overexpressed LGG-1 accumulating in an unprocessed form in aggregates[46, 49, 50]. This is
298 quite different from the reduced levels of mNG::LGG-1 fluorescence we observed in *rme-8*, *dyn-*
299 *1*, *bec-1*, and *vps-15* mutants, where dimmer mNG::LGG-1 is found in more numerous small
300 puncta within the touch neuron soma (Figure 6A). Taken together we interpret the *rme-8*
301 mutant phenotype as reduced but not blocked neuronal autophagy, potentially as an indirect
302 consequence of defective ALR.
303

bioRxiv preprint doi: https://doi.org/10.1101/2023.02.27.530319; this version posted February 28, 2023. The copyright holder for this preprint (which was not certified by peer review) is the author/funder, who has granted bioRxiv a license to display the preprint in perpetuity. It is made available under aCC-BY 4.0 International license.

Another possibility is that defective autophagy initiation is sufficient to produce a *rme-8*-like lysosome phenotype with accumulation of long lysosomal tubules. However, when we measured LMP-1::mNG tubule length in *epg-1(0), epg-6(0), epg-8(0)* and *atg-18(0)* mutants in the touch neurons, we did not find any significant elongation of LMP-1 tubules (Figure 3C-D). These results suggest that a simple block in autophagy initiation is not sufficient to produce this phenotype.

Neuronal autophagic flux requires RME-8/DNAJC13 in mammalian neurons

Given our results in *C. elegans*, we examined the effects of RME-8/DNJC13 on autophagic flux in primary mouse cortical neurons. Similar to our observations in *C. elegans* neurons, we found that autophagic vacuole (AV) density per soma, as visualized by GFP-LC3, was decreased in RME-8/DNAJC13 shRNA neurons compared to controls (Figure 7A, quantified in 7B). We also measured AV density in the presence of pepstatin and E64D, lysosomal protease inhibitors, which block the autolysosome-mediated degradation of autophagic cargo, including GFP-LC3. This type of analysis is often used to judge levels of autophagic flux, since reduced GFP-LC3 levels can result from reduced autophagy, or increased lysosomal degradation of autophagic cargo. If autophagic flux is reduced, then GFP-LC3 levels should also be reduced, even when lysosomal degradation is blocked. However, if GFP-LC3 levels are reduced due to increased lysosomal activity, blocking such lysosomal activity should block the observed GFP-LC3 reduction. We found GFP-LC3 AV density was still decreased in RME-8 shRNA neurons treated with pepstatin (Fig 7A-B). We interpret these results to indicate reduced autophagic flux in

bioRxiv preprint doi: https://doi.org/10.1101/2023.02.27.530319; this version posted February 28, 2023. The copyright holder for this preprint (which was not certified by peer review) is the author/funder, who has granted bioRxiv a license to display the preprint in perpetuity. It is made available under aCC-BY 4.0 International license.

RME-8/DNAJC13-deficient mammalian neurons, potentially at an early stage in autophagy initiation or autophagosome formation.

RME-8, BEC-1/beclin, and VPS-15 are required for efficient clathrin recruitment to autolysosomes

One key molecule associated with the biogenesis of autolysosome reformation tubules is clathrin[2, 4, 38]. Previously, we and other groups had identified an important role for RME-8 in controlling clathrin levels on endosomes in non-neuronal cells [23, 51]. Thus, we hypothesized that RME-8 activity might be important for controlling lysosomal clathrin levels relevant to ALR in neurons. To test this idea we established touch neuron-specific lines expressing clathrin light chain tagged with mNeonGreen (CLIC-1::mNG). We found that CLIC-1::mNG was clearly enriched on LMP-1::mSc labeled lysosomes, supporting a conserved role for clathrin in lysosome homeostasis (Figure 8A-B). Furthermore, we found that *bec-1* and *vps-15,* mutants that accumulate long autolysosomal tubules like *rme-8,* displayed significantly less recruitment of CLIC-1::mNG to neuronal LMP-1-positive lysosomes than controls. Importantly, we found that *rme-8* mutants display an even more severe deficit in CLIC-1::mNG recruitment to LMP-1-positive lysosomes than *bec-1* or *vps-15* mutants (Figure 8A-B). Notably, the severely elongated LMP-1::mSc tubules in *rme-8(b1023ts)* mutants completely lack CLIC-1::mNG labeling. We also identified a defect in clathrin recruitment to neuronal lysosomes in *snx-1* mutants (Figure 8A-B). These mutants are missing RME-8 partner protein SNX-1 (Sorting Nexin 1) that promotes RME-8 activity [15, 24]. BEC-1 and VPS-15 may also be required for efficient RME-8 function, since RME-8 has been reported to have an N-terminal PI(3)P binding domain[21, 51]. Overall, we find

bioRxiv preprint doi: https://doi.org/10.1101/2023.02.27.530319; this version posted February 28, 2023. The copyright holder for this preprint (which was not certified by peer review) is the author/funder, who has granted bioRxiv a license to display the preprint in perpetuity. It is made available under aCC-BY 4.0 International license.

that RME-8, SNX-1, BEC-1, and VPS-15 are required for efficient recruitment of clathrin to neuronal lysosomes. Since clathrin has been reported to be a key molecule in ALR tubule biogenesis, reduced levels of clathrin on lysosomes may lead to defective ALR.

DISCUSSION

Autophagic engulfment of cytoplasmic content represents a major pathway required for maintaining cellular proteostasis and organelle integrity, as well as survival under nutrient deprivation conditions. Autophagy is likely to be especially important in neurons, which tend to be extremely long-lived and cannot divide, and thus lack an effective mechanism to dilute protein aggregates and defective organelles as rapidly dividing cells can. Consistent with this idea, neurons maintain a relatively high basal rate of autophagy, and autophagic dysfunction has been repeatedly implicated in neurodegenerative disease (reviewed in [7, 9, 37, 52, 53]).

Once autophagosomes engulf their cargo they must fuse with lysosomes, producing autolysosomes that degrade their contents. Maintaining a pool of active lysosomes to receive autophagic cargo requires efficient recovery of membrane and other machinery from autolysosomes to reform fresh lysosomes. Defective autolysosome reformation is emerging as an important disease mechanism in its own right, associated with inflammatory and liver disease, muscular dystrophy, metabolic syndrome, Charcot-Marie-Tooth disease, lysosome storage disease, and neurodegenerative disorders such as hereditary spastic paraplegia and Parkinson's disease.

bioRxiv preprint doi: https://doi.org/10.1101/2023.02.27.530319; this version posted February 28, 2023. The copyright holder for this preprint (which was not certified by peer review) is the author/funder, who has granted bioRxiv a license to display the preprint in perpetuity. It is made available under aCC-BY 4.0 International license.

Given the genetic connections suggesting linkage of human RME-8/DNAJC13 to Parkinson's disease and essential tremor, we sought to analyze the requirement for RME-8 in *C. elegans* and mouse neurons. Our experiments identified an important and conserved role of RME-8 in autolysosome reformation in both systems. Loss of RME-8 produced enlarged autolysosomes bearing persistently elongated membrane tubules indicative of a defect in ALR tubule fission to release protolysosomes. In the case of RME-8/DNAJC13 depleted mouse cortical neurons we could document a loss of LC3-negative lysosomes, further indicating a failure in lysosome reformation. We also noted in *C. elegans* bearing an endogenous *rme-8(N861S)* allele, equivalent to human PD-associated allele N855S, an age-dependent effect on RAB-7-positive tubule accumulation, suggested that disease effects could derive from weak dysfunction in ALR.

Extended analysis in the *C. elegans* system revealed a striking loss of clathrin from neuronal autolysosomes, suggesting that clathrin malfunction may underlie the ALR defects when RME-8 is missing. Interestingly we also observed reduced lysosome-associated clathrin in mutants lacking RME-8 partner SNX-1, as well as mutants lacking PI3-kinase complex proteins VPS-15/P150 and BEC-1/beclin. While PI(3)P generated by Vps34 under the control of VPS-15 and BEC-1 homologs was previously linked to ALR, an effect on clathrin was unexpected, since autolysosomal clathrin is thought to assemble with the AP2 clathrin adapter on PI(4,5)P2 enriched membranes. However, RME-8 is known to bind to PI(3)P and to affect clathrin dynamics, likely due to its activity as a Hsc70 co-chaperone, so RME-8 could be a key effector of PI(3)P during ALR[23, 24]. Previous work indicated that *bec-1* mutants affected RME-8 recruitment to membranes in the *C. elegans* intestine [42]. A complex containing ZFYVE26,

bioRxiv preprint doi: https://doi.org/10.1101/2023.02.27.530319; this version posted February 28, 2023. The copyright holder for this preprint (which was not certified by peer review) is the author/funder, who has granted bioRxiv a license to display the preprint in perpetuity. It is made available under aCC-BY 4.0 International license.

391 SPG11, and AP-5 has been proposed as a PI(3)P effector during ALR, but *C. elegans* lacks
392 homologs for any of these proteins, so they cannot explain the conserved requirement from *C.*
393 *elegans* to mammals for PI(3)P during ALR[11, 54].
394
395 Elegant experiments by Rong et al., 2012 suggested dual roles for clathrin in ALR[2]. These
396 authors found that when they depleted PI(4,5)P2 and clathrin from the vesicular body of the
397 autolysosome, tubule budding failed. Alternatively, when PI(4,5)P2 and clathrin were depleted
398 from the tubule, tubule fission failed, blocking protolysosome release. Other work also
399 implicates clathrin regulation in ALR. For instance, abnormally high autolysosome PI(4,5)P2
400 levels were found to result in increased clathrin on elongated ALR tubules, suggesting that
401 general dysregulation of clathrin on tubules may be sufficient inhibit tubule release.
402
403 While we did not observe high-level constitutive residence of RME-8 protein on lysosomes,
404 RME-8 could be present quite transiently, as are some proteins that act in late stages of vesicle
405 budding. If so, RME-8 could play a direct role in clathrin dynamics regulating ALR. While DNAJ-
406 domain co-chaperone auxilin is best known for uncoating clathrin from clathrin-coated vesicles,
407 *in vitro* auxilin promotes clathrin assembly, and has also been proposed to provide co-
408 chaperone activity that helps rearrange clathrin coats from flat to curved during budding[55].
409 RME-8 could act similarly on autolysosomes. RME-8 could also play an indirect role via global
410 clathrin metabolism, as our previous work identified a requirement for RME-8 in uncoating
411 clathrin reservoirs on endosomes, such that loss of RME-8 activity could reduce soluble,

bioRxiv preprint doi: https://doi.org/10.1101/2023.02.27.530319; this version posted February 28, 2023. The copyright holder for this preprint (which was not certified by peer review) is the author/funder, who has granted bioRxiv a license to display the preprint in perpetuity. It is made available under aCC-BY 4.0 International license.

412 cytosolic clathrin levels in the cell needed for assembly on autolysosomes. More analysis will be
413 required to distinguish between these possibilities.
414
415 While it is not clear how clathrin contributes to tubule release, clathrin/AP2 assembly likely acts
416 as a precursor to the recruitment of dynamin, the pinchase thought to directly sever ALR
417 tubules, as it does during clathrin-mediated endocytosis[56]. Effects on dynamin may also
418 underlie some of the effects on ALR that we observed in mutants defective in PI3-kinase
419 regulators BEC-1/beclin and VPS-15/P150. Munson et al found that when a lysosomal pool of
420 PI(3)P is reduced by inhibition of the Vps34 complex, long ALR tubules accumulate[6, 57].
421 PI(3,5)P2 produced from PI(3)P on late endosomes by the PIKFyve complex is also important for
422 neuronal lysosome function and may contribute to ALR [58, 59]. It is unclear to what extent
423 dynamin requires PI(3)P and/or PI(3,5)P2 for its function, but *in vitro* the dynamin PH-domain
424 binds multiple phosphoinositides, including PI(3)P, PI(3,5)P2, and PI(4,5)P2 [60]. Furthermore,
425 *in vitro* PI(3)P and PI(3,5)P2 shows high efficiency in stimulating assembly-dependent GTPase
426 activity by dynamin in complex with its partner Snx9, which also displays broad
427 phosphoinositide binding [61]. Phagocytosis studies have expanded upon this idea *in vivo*,
428 indicating a need for precise and sequential regulation of PI(4,5)P2 and PI(3)P in phagosome
429 release from the plasma membrane mediated by dynamin and Snx9/LST-4[62-64]. Similar
430 regulation may be required on ALR tubules for dynamin-mediated protolysosome release.
431
432 In addition to effects on ALR, we also noted an apparent defect in autophagy, with strongly
433 reduced levels of LGG-1/LC3 in the neuronal soma of *rme-8*, *bec-1/beclin*, *vps-15/P150*, and

bioRxiv preprint doi: https://doi.org/10.1101/2023.02.27.530319; this version posted February 28, 2023. The copyright holder for this preprint (which was not certified by peer review) is the author/funder, who has granted bioRxiv a license to display the preprint in perpetuity. It is made available under aCC-BY 4.0 International license.

434 *dyn-1/dynamin* mutants. This was particularly surprising in the case of DYN-1, since dynamin
435 has not been proposed to have any role in autophagosome formation. Our data argue against
436 the ALR tubule accumulation defects we observed for these mutants being an indirect effect of
437 reduced autophagic flux, as we did not observe tubule accumulation in mutants that affect
438 autophagy initiation but that have no known role in ALR. Results vary in the literature as to
439 whether ALR is required to maintain autophagosome formation rates, but our data supports
440 such a requirement. It seems likely that ALR is required to recycle some component(s) or
441 regulator(s) of autophagy from autolysosomes, and that extended failure in ALR leads to
442 reduced rates of autophagy. An interesting candidate for a recycling cargo during ALR is Atg9,
443 the only transmembrane regulator of autophagy initiation. Atg9 was recently shown to be
444 recycled from autolysosomes by the recycler complex, and RME-8 has also been implicated in
445 Atg9 trafficking [65, 66]. It will be of great interest to further analyze the mechanism of RME-8
446 function in ALR, and to gain further insight into mechanisms by which ALR could influence
447 autophagic flux.
448
449
450 **MATERIALS AND METHODS**

451 All *C. elegans* strains were derived originally from the wild-type Bristol strain N2. Worm
452 cultures, genetic crosses, and other *C. elegans* husbandry were performed according to
453 standard methods[67]. Since the experiments utilized temperature sensitive strains, all strains
454 were maintained at 15°C. A complete list of strains used in this study can be found in Table S1.
455 Every strain listed was created in the Grant Lab for use in this study.

bioRxiv preprint doi: https://doi.org/10.1101/2023.02.27.530319; this version posted February 28, 2023. The copyright holder for this preprint (which was not certified by peer review) is the author/funder, who has granted bioRxiv a license to display the preprint in perpetuity. It is made available under aCC-BY 4.0 International license.

456

457 **Construction of *C. elegans* plasmids**

458 *C. elegans* expression plasmids utilized the Pmec-7 promoter from the *mec-7* gene for touch
459 neuron expression[68]. Vector details are available upon request. Cloning was performed using
460 the Gateway *in vitro* recombination system (Invitrogen, Carlsbad, CA) using Grant lab-modified
461 versions of MiniMos enabled vectors pCFJ1662 (Hygromycin resistant; Addgene #51482) and
462 pCFJ910 (G418 resistant; Addgene #44481) (gifts of Erik Jorgensen, University of Utah):
463 pCFJ1662 Pmec-7 GTWY mNeonGreen let858 (34F6); pCFJ1662 Pmec-7 mNeonGreen GTWY
464 let858 (34D4); pCFJ1662 Pmec-7 GTWY oxGFP let858 (36G3); pCFJ910 Pmec-7 mScarleti GTWY
465 let858 (33B6); and pCFJ910 pmec-7 GTWY mScarleti (35D2). pDONR221 entry vectors
466 containing coding regions for *rab-7*, *lmp-1, lgg-1, clic-1, snx-1, rme-8,* were recombined into
467 neuronal destination vectors by Gateway LR clonase II reaction to generate C-/N- terminal
468 fusions. Single-copy integrations were obtained by MiniMOS technology [69].

469 **Image acquisition and Analysis in *C. elegans***

470 Prior to imaging, L4 hermaphodites maintained at 15°C were picked to fresh OP50 plates and
471 plates were temperature shifted to 25°C (nonpermissive temperature for *rme-8[b1023ts]*) for
472 24-30 h prior to imaging. Live animals were picked into 2 uL of 10 mM levamisole on the center
473 of a cover slip. After two minutes, 5% agarose pads were placed on top. Fluorescence images
474 were obtained using a spinning-disk confocal imaging system: Zeiss Axiovert Z1 microscope
475 equipped with X-Light V2 Spinning Disk Confocal Unit (CrestOptics), 7-line LDI Laser Launch (89
476 North), Prime 95B Scientific CMOS camera (Photometrics) and oil-immersion objective (100X).

bioRxiv preprint doi: https://doi.org/10.1101/2023.02.27.530319; this version posted February 28, 2023. The copyright holder for this preprint (which was not certified by peer review) is the author/funder, who has granted bioRxiv a license to display the preprint in perpetuity. It is made available under aCC-BY 4.0 International license.

Fluorescence images were captured using Metamorph 7.10 software. Z series of 25-30 optical sections were acquired using a 0.2µm step size in order to image through the entire soma. Exposure times ranged from 50ms to 300 ms based on the fluorescent protein being imaged such that images acquired were at minimum in the 12-bit and did not become saturated in the 16-bit range in any genetic background.

Intensity and Length measurements

All data quantification was done using Metamorph 7.10 and data was recorded into Excel. Maximum projections were generated from Z series captured under identical acquisition parameters for each experiment. For each experiment, maximum projections were scaled identically prior to thresholding or length analysis. Puncta within the soma, dendrite, and proximal axon (within ~30um of the soma) were manually thresholded and the average, maximum, and integrated intensity measurements recorded using Metamorph's "Region Measurements" tool. Each worm was treated as one data point.

Maximum projections were also used for length measurements. Lengths were measured and recorded using Metamorph's "region measurements" and using the line tool to trace the length of every puncta/ tubule in the axon. The length of every visible puncta/ tubule within each axon was measured and counted as a data point. Analysis of tubule elongation was restricted to axons due to the poor spatial resolution of puncta within the soma. For each experiment and genetic background, 15-25 animals were analyzed.

Colocalization analysis was performed using MetaMorph 7.7 colocalization plugin, whereby intensities in each channel were thresholded and analyzed.

bioRxiv preprint doi: https://doi.org/10.1101/2023.02.27.530319; this version posted February 28, 2023. The copyright holder for this preprint (which was not certified by peer review) is the author/funder, who has granted bioRxiv a license to display the preprint in perpetuity. It is made available under aCC-BY 4.0 International license.

499

500 **Mouse cortical neuron plasmids and reagents**

501 DNAJC13 shRNA plasmid(sc-77968-SH) and Control shRNA Plasmid-A(sc-108060) were from
502 Santa Cruz Biotechnology. GFP-LC3B, GFP-LAMP1, and mRFP-LC3 constructs were prepared as
503 previously described[70-76]). E64D (Cat. 330005), and Pepstatin A (Cat.516481) (Sigma).

504

505 **Transfection of cultured cortical neurons**

506 Cortices were dissected from E18–19 mouse embryos as described[77-79]). Cortical neurons
507 were dissociated by papain (Worthington, Lakewood, NJ) and plated at a density of 100,000
508 cells per cm^2 on polyornithine- and fibronectin-coated coverslips. Neurons were grown
509 overnight in a plating medium (5% FBS, insulin, glutamate, G5, and B27) supplemented with
510 100× L-glutamine in Neurobasal medium (Invitrogen). Starting at DIV2, cultures were
511 maintained in a conditioned medium with half-feed changes of neuronal feed (B27 in
512 Neurobasal medium) every 3 days. Neurons were co-transfected with Control shRNA (Cat. sc-
513 108060) or DnaJC13 (RME-8) shRNA (Santa Cruz, Cat. sc-77968-SH) with GFP-LC3, GFP-LAMP1,
514 or GFP-LAMP1 and mRFP-LC3 at DIV5 using Lipofectamine 2000 (Invitrogen) before live-cell
515 imaging 7–12 days after transfection before quantification analysis. For some experiments, 24-
516 hour incubation with lysosomal inhibitors E64D (40 μM) and Pepstatin A (40 μM) was applied to
517 suppress lysosomal degradation.

518

519 **Image acquisition and quantification in cultured neurons**

bioRxiv preprint doi: https://doi.org/10.1101/2023.02.27.530319; this version posted February 28, 2023. The copyright holder for this preprint (which was not certified by peer review) is the author/funder, who has granted bioRxiv a license to display the preprint in perpetuity. It is made available under aCC-BY 4.0 International license.

For live-cell imaging, cells were transferred to Tyrode's solution containing 10 mM HEPES, 10 mM glucose, 1.2 mM $CaCl_2$, 1.2 mM $MgCl_2$, 3 mM KCl, and 145 mM NaCl, pH 7.4. The temperature was maintained at 37°C with an air stream incubator. Confocal images were obtained using an Olympus FV3000 oil immersion 60x oil immersion lens (1.3 numerical aperture) with a sequential-acquisition setting, using 488 nm excitation for GFP-LC3 or GFP-LAMP1 and 543 nm for mRFP-LC3. Images were acquired using the same settings below saturation at a resolution of 1,024 x 1,024 pixels (8-bit). Eight to ten sections were taken from the top-to-bottom of the specimen and brightest point projections were made. Time-lapse sequences of 1,024 x 1,024 pixels (8 bit) were collected at 2 s intervals with 1% intensity of the laser to minimize laser-induced bleaching and cell damage while maximizing pinhole opening. Time-lapse images were captured at a total of 100 frames. All recordings started 6 min after the coverslip was placed in the chamber. Images were imported to Adobe Photoshop and morphometric measurements were performed using NIH ImageJ. The thresholds in all images were set to similar levels. Measured data were imported into Excel software for analysis. Data were obtained from at least three independent experiments.

Graphing and Statistics

All results were graphed using GraphPad Prism 9 software, generating scatter plots depicting individual data points. Bars represent mean with SEM. Significance was measured by Student's unpaired t-test when comparing 2 strains/conditions or Ordinary one-way ANOVA when comparing >2 strains, unless otherwise noted. Data were considered statistically different at P <

bioRxiv preprint doi: https://doi.org/10.1101/2023.02.27.530319; this version posted February 28, 2023. The copyright holder for this preprint (which was not certified by peer review) is the author/funder, who has granted bioRxiv a license to display the preprint in perpetuity. It is made available under aCC-BY 4.0 International license.

0.05. P < 0.05 is indicated with single asterisks, P < 0.01 with double asterisks, P < 0.001 with triple asterisks, and P < 0.0001 with quadruple asterisks.

Supplementary Table 1: *C. elegans* Strains used in this study

	Genotype	Figure
RT3799	pwSi113 [pmec-7mScarleti RAB-7 (genomic) let858]	1
RT3972	pwSi113 [pmec-7mScarleti RAB-7 (genomic) let858]; *rme-8(b1023ts)*	1
RT3970	pwSi113 [pmec-7mScarleti RAB-7 (genomic) let858]; *rme-8(pw22[N861S])*	1
RT4061	pwSi225[Pmec-7 LMP-1 mNeonGreen let858 3'UTR]	1
RT4063	pwSi225[Pmec-7 LMP-1 mNeonGreen let858 3'UTR]; *rme-8(b1023ts)*	1
RT4056	pwSi222[Pmec-7 LMP-1 mScarlet let858 3'UTR]	1
RT4058	pwSi222[Pmec-7 LMP-1 mScarlet let858 3'UTR]; *rme-8(b1023ts)*	1
RT4634	pwSi222[Pmec-7 LMP-1 mScarlet let858 3'UTR]; pwSi495[Pmec-7 RME-8oxGFP let858]	1
RT4088	pwSi161[Pmec-7 mNeonGreen LGG-1(cDNA)let858 3'UTR]; pwSi222[Pmec-7 LMP-1 mScarlet let858 3'UTR]	2
RT4089	pwSi161[Pmec-7 mNeonGreen LGG-1(cDNA)let858 3'UTR]; pwSi222[Pmec-7 LMP-1 mScarlet let858 3'UTR]; *rme-8(b1023ts)*	2
RT3969	pwSi161[Pmec-7 mNeonGreen LGG-1(cDNA) let858 3'UTR]	2

bioRxiv preprint doi: https://doi.org/10.1101/2023.02.27.530319; this version posted February 28, 2023. The copyright holder for this preprint (which was not certified by peer review) is the author/funder, who has granted bioRxiv a license to display the preprint in perpetuity. It is made available under aCC-BY 4.0 International license.

RT3971	pwSi161[Pmec-7 mNeonGreen LGG-1(cDNA) let858 3'UTR]; *rme-8(b1023ts)*	2
RT3970	pwSi161[Pmec-7 mNeonGreen LGG-1(cDNA) let858 3'UTR]; *rme-8(pw22[N861S])*	2
RT4077	pwSi161[Pmec-7 mNeonGreen LGG-1(cDNA) let858 3'UTR]; *snx-1(tm847)*	2
RT4581	pwSi225[Pmec-7 LMP-1 mNeonGreen let858 3'UTR]; *vps-15(or1235ts)*	3
RT4580	pwSi225[Pmec-7 LMP-1 mNeonGreen let858 3'UTR]; *bec-1(ok691) IV/nT1 [qIs51]*	3
RT4582	pwSi225[Pmec-7 LMP-1 mNeonGreen let858 3'UTR]; *dyn-1(ky51ts)*	3
RT4583	pwSi225[Pmec-7 LMP-1 mNeonGreen let858 3'UTR]; *epg-8(bp251)*	3
RT4499	pwSi225[Pmec-7 LMP-1 mNeonGreen let858 3'UTR]; *atg-18(gk378)*	3
RT4644	pwSi225[Pmec-7 LMP-1 mNeonGreen let858 3'UTR]; *epg-1(bp414)*	3
RT4645	pwSi225[Pmec-7 LMP-1 mNeonGreen let858 3'UTR]; *epg-6(bp242)*	3
RT4637	pwSi222[Pmec-7 LMP-1 mScarlet let858 3'UTR]; pwSi495[Pmec-7 RME-8oxGFP let858]; *rme-8(b1023ts)*	5
RT4635	pwSi495[Pmec-7 RME-8::GFP let858]; pwSi503 [Pmec-7 mScarleti SNX-1 cDNA let858]	5
RT4573	pwSi161[Pmec-7 mNeonGreen LGG-1(cDNA) let858 3'UTR]; *vps-15(or1235ts)*	6
RT4500	pwSi161[Pmec-7 mNeonGreen LGG-1(cDNA) let858 3'UTR; *bec-1(ok691) IV/nT1 [qIs51]*	6

bioRxiv preprint doi: https://doi.org/10.1101/2023.02.27.530319; this version posted February 28, 2023. The copyright holder for this preprint (which was not certified by peer review) is the author/funder, who has granted bioRxiv a license to display the preprint in perpetuity. It is made available under aCC-BY 4.0 International license.

RT4574	pwSi161[Pmec-7 mNeonGreen LGG-1(cDNA) let858 3'UTR]; *dyn-1(ky51ts)*	6
RT4575	pwSi161[Pmec-7 mNeonGreen LGG-1(cDNA) let858 3'UTR]; *epg-8(bp251)*	6
RT4486	pwSi161[Pmec-7 mNeonGreen LGG-1(cDNA) let858 3'UTR]; *epg-6(bp242); him-5 (e1490)*	6
RT4487	pwSi161[Pmec-7 mNeonGreen LGG-1(cDNA) let858 3'UTR]; *epg-1(bp414)*	6
RT4427	pwSi222 [Pmec-7 LMP-1 mScarleti let858 3'UTR]; pwSi345[Pmec-7 clic-1 mNeonGreen let858 3'UTR]	8
RT4428	pwSi222 [Pmec-7 LMP-1 mScarleti let858 3'UTR]; pwSi345[Pmec-7 clic-1 mNeonGreen let858 3'UTR]; *rme-8(b1023ts)*	8
RT4604	pwSi222 [Pmec-7 LMP-1 mScarleti let858 3'UTR]; pwSi345[Pmec-7 clic-1 mNeonGreen let858 3'UTR]; *rme-8(pw22[N861S])*	8
RT4593	pwSi222 [Pmec-7 LMP-1 mScarleti let858 3'UTR]; pwSi345[Pmec-7 clic-1 mNeonGreen let858 3'UTR]; *snx-1(tm847)*	8
RT4594	pwSi222 [Pmec-7 LMP-1 mScarleti let858 3'UTR]; pwSi345[Pmec-7 clic-1 mNeonGreen let858 3'UTR]; *bec-1(ok691) IV/nT1 [qIs51]*	8
RT4595	pwSi222 [Pmec-7 LMP-1 mScarleti let858 3'UTR]; pwSi345[Pmec-7 clic-1 mNeonGreen let858 3'UTR]; *vps-15(or1235ts)*	8
RT4636	pwSi495[Pmec-7 RME-8oxGFP let858]; pwSi499 [Pmec-7 clic-1 mScarleti let858]	8

Acknowledgments

bioRxiv preprint doi: https://doi.org/10.1101/2023.02.27.530319; this version posted February 28, 2023. The copyright holder for this preprint (which was not certified by peer review) is the author/funder, who has granted bioRxiv a license to display the preprint in perpetuity. It is made available under aCC-BY 4.0 International license.

We would like to thank the Grant lab for critical comments and suggestions. We thank Peter Schweinsberg and Ge Bai for technical assistance in plasmid construction, and Helen Ushakov for expert microinjection. We thank Alicia Melendez for expert advice and ideas. This work was supported by NIH Grant 5R01GM135326 to B.D.G.

Figure Legends

Figure 1. Loss of RME-8 results in accumulation of elongated lysosomal tubules.

A) Representative drawing of ALM neurons in *C. elegans*. One of two ALM neurons is shown (other is located laterally opposite). Black dashed box represents the approximate area that is shown in example micrographs. **B)** Fluorescent micrographs showing pmec-7 promoter-driven mScarletI::RAB-7 labeled (late endosome/ lysosome marker) puncta in soma (left) and proximal axon (right) in ALM neurons in *rme-8(+)*, *rme-8(N861S)*, and *rme-8(b1023ts)* Day 1 adult backgrounds. White arrowhead indicates grossly elongated tubule. **C)** Length of RAB-7 puncta/ tubule in the proximal axon in *rme-8(+)*, *rme-8(N861S)* and *rme-8(b1023ts)* is graphed in Day 1 adult animals. Each data point represents an individual puncta/tubule. A minimum of 15 animals were analyzed per strain. **D)** Pmec-7 promoter-driven mScarletI::RAB-7 labeled puncta in *rme-8(+)* and *rme-8(N861S)* backgrounds in Day 9 adult. **E)** Length of RAB-7 puncta/ tubule in the proximal axon in *rme-8(+)*, and *rme-8(N861S)* is graphed in Day 9 adults. Each data point represents an individual puncta/tubule. **F)** Pmec-7 LMP-1::mNeonGreen (NG) labeled (lysosome marker) puncta. A severely elongated LMP-1 positive tubule can be seen emanating into the axon from puncta in the soma (white arrow), and another dimmer tubule can be seen further

bioRxiv preprint doi: https://doi.org/10.1101/2023.02.27.530319; this version posted February 28, 2023. The copyright holder for this preprint (which was not certified by peer review) is the author/funder, who has granted bioRxiv a license to display the preprint in perpetuity. It is made available under aCC-BY 4.0 International license.

569 out in the axon (white arrowhead). **G)** Quantification of LMP-1::NG axonal puncta/ tubule
570 length seen in conditions shown in E). Each data point represents an individual puncta/tubule. A
571 minimum of 15 animals were analyzed per strain. **H)** Graph depicting LMP-1::mNG Integrated
572 intensity (Arbitrary Units; AU) for the same experiment as 1E and 1F. Each data point
573 represents the integrated intensity of all thresholded puncta in one soma in one animal. **I)**
574 Micrographs of pmec-7 RME-8::oxGFP rescue of LMP-1::mScarleti length in *rme-8(b1023ts)*
575 background. **J)** Graph quantifying elongation of LMP-1::mScarletI in *rme-8(+), rme-8(b1023ts),*
576 and *rme-8(b1023ts); pmec-7 RME-8::GFP.* Scale bars, 5 um. Abbreviations: *rme-8(NS)*= *rme-*
577 *8(pw22[N861S*]); *rme-8(ts)= rme-8(b1023ts).*
578 **C), E),** and **J)**: One-way ANOVA followed with Tukey's Multiple Comparisons Test. **G)**, **H)**:
579 Student's unpaired t-test. *P < 0.05, **P < 0.01, ***P < 0.001, ****P < 0.0001.
580
581 **Figure 2. *rme-8* mutants accumulate abnormal autolysosomes.**
582 **A)** Micrographs are shown for single channels as well as merged images in double-labeled LMP-
583 1::mScarlet-I (lysosome marker); mNG::LGG-1 (autophagosome marker) in *rme-8(+)* and *rme-*
584 *8(b1023ts)* backgrounds. White arrow labels mNG::LGG-1+/ LMP-1::mSc- puncta. White
585 arrowhead labels tubules labeled by LMP-1 and dimly labeled by LGG-1 can be seen in the *rme-*
586 *8(b1023ts)* background. **B)** Graphs quantifying the colocalization of LMP-1:mSc and mNG::LGG-
587 1, measured by %Area Colocalization. Each data point represents average % Area colocalization
588 for one animal. **P < 0.01, ns > 0.05 by two-tailed unpaired t-test.
589 **C)** Micrograph showing pmec-7::mNG::LGG-1 in neurons of *rme-8(+), rme-8(b1023ts), rme-*
590 *8(N861S),* and *snx-1(tm847)* backgrounds. Scale bar: 5um. **D)** Graph quantifying elongation of

bioRxiv preprint doi: https://doi.org/10.1101/2023.02.27.530319; this version posted February 28, 2023. The copyright holder for this preprint (which was not certified by peer review) is the author/funder, who has granted bioRxiv a license to display the preprint in perpetuity. It is made available under aCC-BY 4.0 International license.

591 LGG-1::mNG in *rme-8(+)*, *rme-8(b1023ts)*, and *rme-8(N861S); snx-1(0)* backgrounds. Each data
592 point represents an individual puncta/tubule. ****P < 0.0001 by One-way ANOVA followed
593 with Tukey's Multiple Comparisons Test. **E)** Graph depicting mNG::LGG-1 Integrated intensity
594 (Arbitrary Units; AU) for the same experiment as 2C and 2D. Each data point represents the
595 integrated intensity of all thresholded puncta in one soma in one animal. ****P < 0.0001,
596 **P<0.01 by One-way ANOVA followed with Tukey's Multiple Comparisons Test.
597
598 **Figure 3. Loss of RME-8 phenocopies autolysosome reformation mutants.**
599 **A)** Micrographs are shown of pmec-7 LMP-1::mNG in ALM neurons in *rme-8(+)*, *rme-8(ts)*, *vps-*
600 *15(ts)*, *bec-1(0)*, and *dyn-1(ts)* backgrounds. **B)** Quantification of LMP-1 tubule length (um) in
601 ALM proximal axons in the backgrounds shown in 3A. Each data point represents an individual
602 puncta/tubule. ***P < 0.001, **P < 0.01, *P < 0.05, ns > 0.05 by One-way ANOVA followed with
603 Tukey's Multiple Comparisons Test. **C)** Micrographs are shown of pmec-7 LMP-1::mNG in ALM
604 neurons in *rme-8(+)*, *rme-8(ts)*, *atg-18(0)*, *epg-1(0)*, *epg-6(0)*, *epg-8(0)*, backgrounds. Example
605 images and graphs are separate from 3A and 3B because data was obtained during separate
606 experiments. **D)** Quantification of LMP-1 tubule length (um) in ALM proximal axons in the
607 backgrounds shown in 3C. Each data point represents an individual puncta/tubule. ***P <
608 0.001, **P < 0.01, *P < 0.05, ns > 0.05 by One-way ANOVA followed with Tukey's Multiple
609 Comparisons Test.
610
611

bioRxiv preprint doi: https://doi.org/10.1101/2023.02.27.530319; this version posted February 28, 2023. The copyright holder for this preprint (which was not certified by peer review) is the author/funder, who has granted bioRxiv a license to display the preprint in perpetuity. It is made available under aCC-BY 4.0 International license.

Figure 4. RME-8 knockdown in mouse cortical neurons causes elongated autolysosome tubules and enlarged autolysosomes.

A) Micrographs of double-labeled GFP-LAMP1, mRFP-LC3 in primary mouse cortical neurons transfected with control (top panel) or RME8/DNAJC13 (bottom two panels) shRNA. Images are shown for single channel labeling and merged. Arrows (top panel, control shRNA) indicate lysosomes (GFP-LAMP1 positive; mRFP-LC3 negative), arrowheads indicate autolysosomes (GFP-LAMP1 positive; mRFP-LC3 positive). Scale bar, 10 um.

B) The average LAMP1 tubules length of each soma is quantified in control and RME-8/DNAJC13 shRNA conditions. Each puncta represents the average length in one neuron. **C)** Frequency distribution of average tubule length per soma in control and RME-8/DNAJC13 shRNA. **D)** Frequency distribution of LAMP-1 positive (lysosomes and autolysosomes) vesicle area per soma in control and RME-8/DNAJC13 shRNA. **B), F), E):** Student's unpaired t-test. ****P<0.0001.

Figure 5. RME-8 localizes primarily to endosomes.

A) Fluorescent single channel and merged micrographs of double labeled strains LMP-1::mScarlet; RME-8::GFP and mScarlet::SNX-1; RME-8::GFP in wild-type background. Scale bar, 5um. **B)** Quantification of colocalization between strains shown in **A)** using % Area Colocalization.

Figure 6. Loss of RME-8 causes decreased autophagosome levels like known ALR mutants.

bioRxiv preprint doi: https://doi.org/10.1101/2023.02.27.530319; this version posted February 28, 2023. The copyright holder for this preprint (which was not certified by peer review) is the author/funder, who has granted bioRxiv a license to display the preprint in perpetuity. It is made available under aCC-BY 4.0 International license.

A), **D)** Micrographs of pmec-7 LGG-1::mNG in *C. elegans* ALM neurons. Area shown includes soma (left) and proximal axon (right). Example images and graphs are separate because data was obtained during separate experiments. Scale bars, 5 um.

B), **E)** Quantification of integrated intensity of LGG-1::mNG puncta in backgrounds shown in **A)** and **D)** (AU; arbitrary units). **C)**, **F)** Average Intensity of LGG-1 positive puncta in axons and somas of backgrounds shown in **A)** and **D)**. ***P < 0.001, ****P < 0.0001 by One-way ANOVA followed with Tukey's Multiple Comparisons Test.

Figure 7. RME-8/DNAJC13 knock down in mouse cortical neurons reduces autophagic flux.

A) Micrographs are shown of *in vitro* mouse cortical neurons transfected with GFP-LC3. A 2x2 factorial design was used, conditions were treatment with either control or RME-8/DNAJC13 shRNA, and +/- pepstatin/ E64D (lysosome inhibitors; LIs). Scale bar, 10 um. **B)** Autophagic vacuole (AV) density is quantified in neurons for the 2x2 factorial design shown in **A)**. ****P < 0.0001 by Student's t-test.

Figure 8. RME-8 is required for efficient clathrin recruitment to lysosomes.

A) Single-channel and merge images of double-labeled LMP-1::mSc and CLIC-1::mNG in C. elegans' ALM neurons. **B)** Quantification of the percent of LMP-1::mSc that has CLIC-1::mNG present on it. Scale bar, 5 um. One-way ANOVA followed with Tukey's Multiple Comparisons Test. *P < 0.05, **P < 0.01, ***P < 0.001, ****P < 0.0001.

Supplementary Figures

bioRxiv preprint doi: https://doi.org/10.1101/2023.02.27.530319; this version posted February 28, 2023. The copyright holder for this preprint (which was not certified by peer review) is the author/funder, who has granted bioRxiv a license to display the preprint in perpetuity. It is made available under aCC-BY 4.0 International license.

Movie S1. Dynamics of LMP-1::mNG labeled lysosomes in *rme-8(ts) C. elegans* ALM soma shows persistent lysosomal tubulation. Time lapse image sequences of ALM neurons expressing LMP-1 are shown. An elongated tubule emanating from a lysosome vesicle can be seen. The tubules expands and contracts, but does not sever. Images were collected at 1s increments for 45s.

Movie S2. Dynamics of LMP-1::mNG labeled lysosomes in wild-type *C. elegans* ALM soma. Time lapse image sequence of ALM neurons expressing LMP-1 in an *rme-8(+)* background is shown. A lysosome in the lower portion of the soma can be observed producing tiny transient tubular processes. Images were collected at 1s increments for 90s.

Movie S3. Dynamics of lysosomal organelles marked by GFP-LAMP1 in the proximal processes of the cortical neuron expressing DNAJC13(RME-8) shRNA.
Cortical neurons were transfected with GFP-LAMP1 and RME-8/DNAJC13 shRNA at DIV5, followed by time-lapse imaging at DIV16. Note that GFP-LAMP1-indicated lysosomal organelles appear as elongated tubules and undergo oscillatory movement in proximal processes to the neuronal soma (right). Time-lapse sequences were collected at 2-sec intervals during a 200-s observation.

Movie S4. Dynamics of GFP-LAMP-1-labeled lysosomes in the proximal processes of control cortical neuron expressing Control shRNA.
Cortical neurons were transfected with GFP-LAMP1 and Control shRNA at DIV5, followed by time-lapse imaging at DIV16. Note that lysosomal organelles appear as small puncta in the

bioRxiv preprint doi: https://doi.org/10.1101/2023.02.27.530319; this version posted February 28, 2023. The copyright holder for this preprint (which was not certified by peer review) is the author/funder, who has granted bioRxiv a license to display the preprint in perpetuity. It is made available under aCC-BY 4.0 International license.

neuronal process and undergo dynamic movement in a predominant retrograde direction toward the soma (left). Time-lapse sequences were collected at 2-sec intervals during a 200-s observation.

1. Yu, L., et al., *Termination of autophagy and reformation of lysosomes regulated by mTOR.* Nature, 2010. **465**(7300): p. 942-6.
2. Rong, Y., et al., *Clathrin and phosphatidylinositol-4,5-bisphosphate regulate autophagic lysosome reformation.* Nat Cell Biol, 2012. **14**(9): p. 924-34.
3. Schulze, R.J., et al., *Lipid droplet breakdown requires Dynamin 2 for vesiculation of autolysosomal tubules in hepatocytes.* Journal of Cell Biology, 2013. **203**(2): p. 315-326.
4. Du, W., et al., *Kinesin 1 Drives Autolysosome Tubulation.* Dev Cell, 2016. **37**(4): p. 326-336.
5. Eramo, M.J., et al., *Bidirectional interconversion between PtdIns4P and PtdIns(4,5)P2 is required for autophagic lysosome reformation and protection from skeletal muscle disease.* Autophagy, 2021. **17**(5): p. 1287-1289.
6. Munson, M.J., et al., *mTOR activates the VPS34-UVRAG complex to regulate autolysosomal tubulation and cell survival.* Embo j, 2015. **34**(17): p. 2272-90.
7. Boland, B., et al., *Autophagy Induction and Autophagosome Clearance in Neurons: Relationship to Autophagic Pathology in Alzheimer's Disease.* The Journal of Neuroscience, 2008. **28**(27): p. 6926.
8. Maday, S. and E.L. Holzbaur, *Compartment-Specific Regulation of Autophagy in Primary Neurons.* J Neurosci, 2016. **36**(22): p. 5933-45.
9. Takalo, M., et al., *Protein aggregation and degradation mechanisms in neurodegenerative diseases.* Am J Neurodegener Dis, 2013. **2**(1): p. 1-14.
10. Tan, C.-C., et al., *Autophagy in aging and neurodegenerative diseases: implications for pathogenesis and therapy.* Neurobiology of Aging, 2014. **35**(5): p. 941-957.
11. Chang, J., S. Lee, and C. Blackstone, *Spastic paraplegia proteins spastizin and spatacsin mediate autophagic lysosome reformation.* The Journal of Clinical Investigation, 2014. **124**(12): p. 5249-5262.
12. Francis, V., et al., *The ARSACS disease protein sacsin controls lysosomal positioning and reformation by regulating microtubule dynamics.* Journal of Biological Chemistry, 2022. **298**(9).
13. Vilarino-Guell, C., et al., *DNAJC13 mutations in Parkinson disease.* Hum Mol Genet, 2014. **23**(7): p. 1794-801.
14. Appel-Cresswell, S., et al., *Clinical, positron emission tomography, and pathological studies of DNAJC13 p.N855S Parkinsonism.* Mov Disord, 2014. **29**(13): p. 1684-7.

bioRxiv preprint doi: https://doi.org/10.1101/2023.02.27.530319; this version posted February 28, 2023. The copyright holder for this preprint (which was not certified by peer review) is the author/funder, who has granted bioRxiv a license to display the preprint in perpetuity. It is made available under aCC-BY 4.0 International license.

15. Norris, A., et al., *Mutagenesis and structural modeling implicate RME-8 IWN domains as conformational control points.* PLOS Genetics, 2022. **18**(10): p. e1010296.
16. Spillantini, M.G., et al., *α-Synuclein in Lewy bodies.* Nature, 1997. **388**(6645): p. 839-840.
17. Rajput, A., et al., *VPS35 and DNAJC13 disease-causing variants in essential tremor.* Eur J Hum Genet, 2015. **23**(6): p. 887-8.
18. Grant, B. and D. Hirsh, *Receptor-mediated endocytosis in the Caenorhabditis elegans oocyte.* Mol Biol Cell, 1999. **10**(12): p. 4311-26.
19. Zhang, Y., B. Grant, and D. Hirsh, *RME-8, a Conserved J-Domain Protein, Is Required for Endocytosis in Caenorhabditis elegans.* Mol Biol Cell, 2001. **12**(7): p. 2011-21.
20. Greener, T., et al., *Caenorhabditis elegans auxilin: a J-domain protein essential for clathrin-mediated endocytosis in vivo.* Nat Cell Biol, 2001. **3**(2): p. 215-9.
21. Xhabija, B., et al., *Receptor mediated endocytosis 8 is a novel PI(3)P binding protein regulated by myotubularin-related 2.* FEBS Lett, 2011. **585**(12): p. 1722-8.
22. Norris, A. and B.D. Grant, *Endosomal microdomains: Formation and function.* Current Opinion in Cell Biology, 2020. **65**: p. 86-95.
23. Shi, A., et al., *Regulation of endosomal clathrin and retromer-mediated endosome to Golgi retrograde transport by the J-domain protein RME-8.* EMBO J, 2009. **28**(21): p. 3290-302.
24. Norris, A., et al., *SNX-1 and RME-8 oppose the assembly of HGRS-1/ESCRT-0 degradative microdomains on endosomes.* Proc Natl Acad Sci U S A, 2017. **114**(3): p. E307-E316.
25. Hurley, J.H., *The ESCRT complexes.* Crit Rev Biochem Mol Biol, 2010. **45**(6): p. 463-87.
26. Hurley, J.H. and P.I. Hanson, *Membrane budding and scission by the ESCRT machinery: it's all in the neck.* Nat Rev Mol Cell Biol, 2010. **11**(8): p. 556-66.
27. Wollert, T. and J.H. Hurley, *Molecular mechanism of multivesicular body biogenesis by ESCRT complexes.* Nature, 2010. **464**(7290): p. 864-9.
28. Popoff, V., et al., *Analysis of Articulation Between Clathrin and Retromer in Retrograde Sorting on Early Endosomes.* Traffic, 2009. **10**(12): p. 1868-1880.
29. Gagliardi, M., et al., *DNAJC13 mutation screening in patients with Parkinson's disease from South Italy.* Parkinsonism Relat Disord, 2018. **55**: p. 134-137.
30. Gustavsson, E.K., et al., *DNAJC13 genetic variants in parkinsonism.* Mov Disord, 2015. **30**(2): p. 273-8.
31. Lorenzo-Betancor, O., et al., *DNAJC13 p.Asn855Ser mutation screening in Parkinson's disease and pathologically confirmed Lewy body disease patients.* Eur J Neurol, 2015. **22**(9): p. 1323-5.
32. Yoshida, S., et al., *Parkinson's disease-linked DNAJC13 mutation aggravates alpha-synuclein-induced neurotoxicity through perturbation of endosomal trafficking.* Hum Mol Genet, 2018. **27**(5): p. 823-836.
33. Schafer, W.R., *Mechanosensory molecules and circuits in C. elegans.* Pflugers Arch, 2015. **467**(1): p. 39-48.
34. Hamelin, M., et al., *The mec-7 beta-tubulin gene of Caenorhabditis elegans is expressed primarily in the touch receptor neurons.* The EMBO Journal, 1992. **11**(8): p. 2885-2893.
35. Lőrincz, P. and G. Juhász, *Autophagosome-Lysosome Fusion.* Journal of Molecular Biology, 2020. **432**(8): p. 2462-2482.

bioRxiv preprint doi: https://doi.org/10.1101/2023.02.27.530319; this version posted February 28, 2023. The copyright holder for this preprint (which was not certified by peer review) is the author/funder, who has granted bioRxiv a license to display the preprint in perpetuity. It is made available under aCC-BY 4.0 International license.

36. Nguyen, J.A. and R.M. Yates, *Better Together: Current Insights Into Phagosome-Lysosome Fusion.* Frontiers in Immunology, 2021. **12**.
37. Malik, B.R., et al., *Autophagic and endo-lysosomal dysfunction in neurodegenerative disease.* Molecular Brain, 2019. **12**(1): p. 100.
38. McGrath, M.J., et al., *Defective lysosome reformation during autophagy causes skeletal muscle disease.* J Clin Invest, 2021. **131**(1).
39. Serra-Vinardell, J., et al., *LYST deficiency impairs autophagic lysosome reformation in neurons and alters lysosome number and size.* Cellular and Molecular Life Sciences, 2023. **80**(2): p. 53.
40. Cao, Y. and D.J. Klionsky, *Physiological functions of Atg6/Beclin 1: a unique autophagy-related protein.* Cell Research, 2007. **17**(10): p. 839-849.
41. Kihara, A., et al., *Two Distinct Vps34 Phosphatidylinositol 3–Kinase Complexes Function in Autophagy and Carboxypeptidase Y Sorting inSaccharomyces cerevisiae.* Journal of Cell Biology, 2001. **152**(3): p. 519-530.
42. Ruck, A., et al., *The Atg6/Vps30/Beclin 1 ortholog BEC-1 mediates endocytic retrograde transport in addition to autophagy in C. elegans.* Autophagy, 2011. **7**(4): p. 386-400.
43. Clark, S.G., et al., *A dynamin GTPase mutation causes a rapid and reversible temperature-inducible locomotion defect in C. elegans.* Proceedings of the National Academy of Sciences, 1997. **94**(19): p. 10438-10443.
44. Hu, Y. and F. Reggiori, *Molecular regulation of autophagosome formation.* Biochemical Society Transactions, 2022. **50**(1): p. 55-69.
45. Nishimura, T., et al., *Autophagosome formation is initiated at phosphatidylinositol synthase-enriched ER subdomains.* The EMBO Journal, 2017. **36**(12): p. 1719-1735.
46. Tian, E., et al., *epg-1 functions in autophagy-regulated processes and may encode a highly divergent Atg13 homolog in C. elegans.* Autophagy, 2009. **5**(5): p. 608-615.
47. Lu, Q., et al., *The WD40 Repeat PtdIns(3)P-Binding Protein EPG-6 Regulates Progression of Omegasomes to Autophagosomes.* Developmental Cell, 2011. **21**(2): p. 343-357.
48. Yang, P. and H. Zhang, *The coiled-coil domain protein EPG-8 plays an essential role in the autophagy pathway in C. elegans.* Autophagy, 2011. **7**(2): p. 159-165.
49. Kuma, A., M. Matsui, and N. Mizushima, *LC3, an autophagosome marker, can be incorporated into protein aggregates independent of autophagy: caution in the interpretation of LC3 localization.* Autophagy, 2007. **3**(4): p. 323-8.
50. Zhang, H., et al., *Guidelines for monitoring autophagy in Caenorhabditis elegans.* Autophagy, 2015. **11**(1): p. 9-27.
51. Xhabija, B. and P.O. Vacratsis, *Receptor-mediated Endocytosis 8 Utilizes an N-terminal Phosphoinositide-binding Motif to Regulate Endosomal Clathrin Dynamics.* J Biol Chem, 2015. **290**(35): p. 21676-89.
52. Stavoe, A.K.H. and E.L.F. Holzbaur, *Autophagy in Neurons.* Annu Rev Cell Dev Biol, 2019. **35**: p. 477-500.
53. Ferguson, S.M., *Neuronal lysosomes.* Neurosci Lett, 2019. **697**: p. 1-9.
54. Hirst, J., et al., *Rag GTPases and phosphatidylinositol 3-phosphate mediate recruitment of the AP-5/SPG11/SPG15 complex.* Journal of Cell Biology, 2021. **220**(2).
55. Ken Sato, A.N., Miyuki Sato, and Barth D. Grant., *C. elegans as a model for membrane traffic.* WormBook: The Online Review of C. elegans Biology [Internet], 2005-2018.

bioRxiv preprint doi: https://doi.org/10.1101/2023.02.27.530319; this version posted February 28, 2023. The copyright holder for this preprint (which was not certified by peer review) is the author/funder, who has granted bioRxiv a license to display the preprint in perpetuity. It is made available under aCC-BY 4.0 International license.

56. Kirchhausen, T. and S.C. Harrison, *Protein organization in clathrin trimers.* Cell, 1981. **23**(3): p. 755-61.
57. Chen, Y. and L. Yu, *Scissors for autolysosome tubules.* The EMBO Journal, 2015. **34**(17): p. 2217-2218.
58. Lenk, G.M. and M.H. Meisler, *Chapter Fourteen - Mouse Models of PI(3,5)P2 Deficiency with Impaired Lysosome Function*, in *Methods in Enzymology*, P.M. Conn, Editor. 2014, Academic Press. p. 245-260.
59. Rivero-Ríos, P. and L.S. Weisman, *Roles of PIKfyve in multiple cellular pathways.* Current Opinion in Cell Biology, 2022. **76**: p. 102086.
60. Klein, D.E., et al., *The pleckstrin homology domains of dynamin isoforms require oligomerization for high affinity phosphoinositide binding.* J Biol Chem, 1998. **273**(42): p. 27725-33.
61. Yarar, D., et al., *SNX9 Activities are Regulated by Multiple Phosphoinositides Through both PX and BAR Domains.* Traffic, 2008. **9**(1): p. 133-146.
62. Lu, N., et al., *Three sorting nexins drive the degradation of apoptotic cells in response to PtdIns(3)P signaling.* Mol Biol Cell, 2011. **22**(3): p. 354-74.
63. Lu, N., et al., *Two PI 3-Kinases and One PI 3-Phosphatase Together Establish the Cyclic Waves of Phagosomal PtdIns(3)P Critical for the Degradation of Apoptotic Cells.* PLOS Biology, 2012. **10**(1): p. e1001245.
64. Cheng, S., et al., *PtdIns(4,5)P_2 and PtdIns3P coordinate to regulate phagosomal sealing for apoptotic cell clearance.* J Cell Biol, 2015. **210**(3): p. 485-502.
65. Zhou, C., et al., *Recycling of autophagosomal components from autolysosomes by the recycler complex.* Nat Cell Biol, 2022. **24**(4): p. 497-512.
66. Besemer, A.S., et al., *Receptor-mediated endocytosis 8 (RME-8)/DNAJC13 is a novel positive modulator of autophagy and stabilizes cellular protein homeostasis.* Cell Mol Life Sci, 2021. **78**(2): p. 645-660.
67. Brenner, S., *The genetics of Caenorhabditis elegans.* Genetics, 1974. **77**(1): p. 71-94.
68. Hamelin, M., et al., *The mec-7 beta-tubulin gene of Caenorhabditis elegans is expressed primarily in the touch receptor neurons.* EMBO J, 1992. **11**(8): p. 2885-93.
69. Frokjaer-Jensen, C., et al., *Single-copy insertion of transgenes in Caenorhabditis elegans.* Nat Genet, 2008. **40**(11): p. 1375-83.
70. Cai, Q., et al., *Snapin-Regulated Late Endosomal Transport Is Critical for Efficient Autophagy-Lysosomal Function in Neurons.* Neuron, 2010. **68**(1): p. 73-86.
71. Cai, Q., et al., *Spatial Parkin Translocation and Degradation of Damaged Mitochondria via Mitophagy in Live Cortical Neurons.* Current Biology, 2012. **22**(6): p. 545-552.
72. Ye, X. and Q. Cai, *Snapin-Mediated BACE1 Retrograde Transport Is Essential for Its Degradation in Lysosomes and Regulation of APP Processing in Neurons.* Cell Reports, 2014. **6**(1): p. 24-31.
73. Ye, X., et al., *Parkin-mediated mitophagy in mutant hAPP neurons and Alzheimer's disease patient brains.* Human Molecular Genetics, 2015. **24**(10): p. 2938-2951.
74. Ye, X., et al., *Regulation of Synaptic Amyloid-β Generation through BACE1 Retrograde Transport in a Mouse Model of Alzheimer's Disease.* The Journal of Neuroscience, 2017. **37**(10): p. 2639-2655.

bioRxiv preprint doi: https://doi.org/10.1101/2023.02.27.530319; this version posted February 28, 2023. The copyright holder for this preprint (which was not certified by peer review) is the author/funder, who has granted bioRxiv a license to display the preprint in perpetuity. It is made available under aCC-BY 4.0 International license.

75. Feng, T., et al., *Autophagy-mediated Regulation of BACE1 Protein Trafficking and Degradation**. Journal of Biological Chemistry, 2017. **292**(5): p. 1679-1690.
76. Tammineni, P., et al., *Impaired axonal retrograde trafficking of the retromer complex augments lysosomal deficits in Alzheimer's disease neurons.* Hum Mol Genet, 2017. **26**(22): p. 4352-4366.
77. Han, S., et al., *The role of mitophagy in the regulation of mitochondrial energetic status in neurons.* Autophagy, 2021. **17**(12): p. 4182-4201.
78. Han, S., et al., *Mitophagy regulates integrity of mitochondria at synapses and is critical for synaptic maintenance.* EMBO Rep, 2020. **21**(9): p. e49801.
79. Jeong, Y.Y., et al., *Broad activation of the Parkin pathway induces synaptic mitochondrial deficits in early tauopathy.* Brain, 2022. **145**(1): p. 305-323.

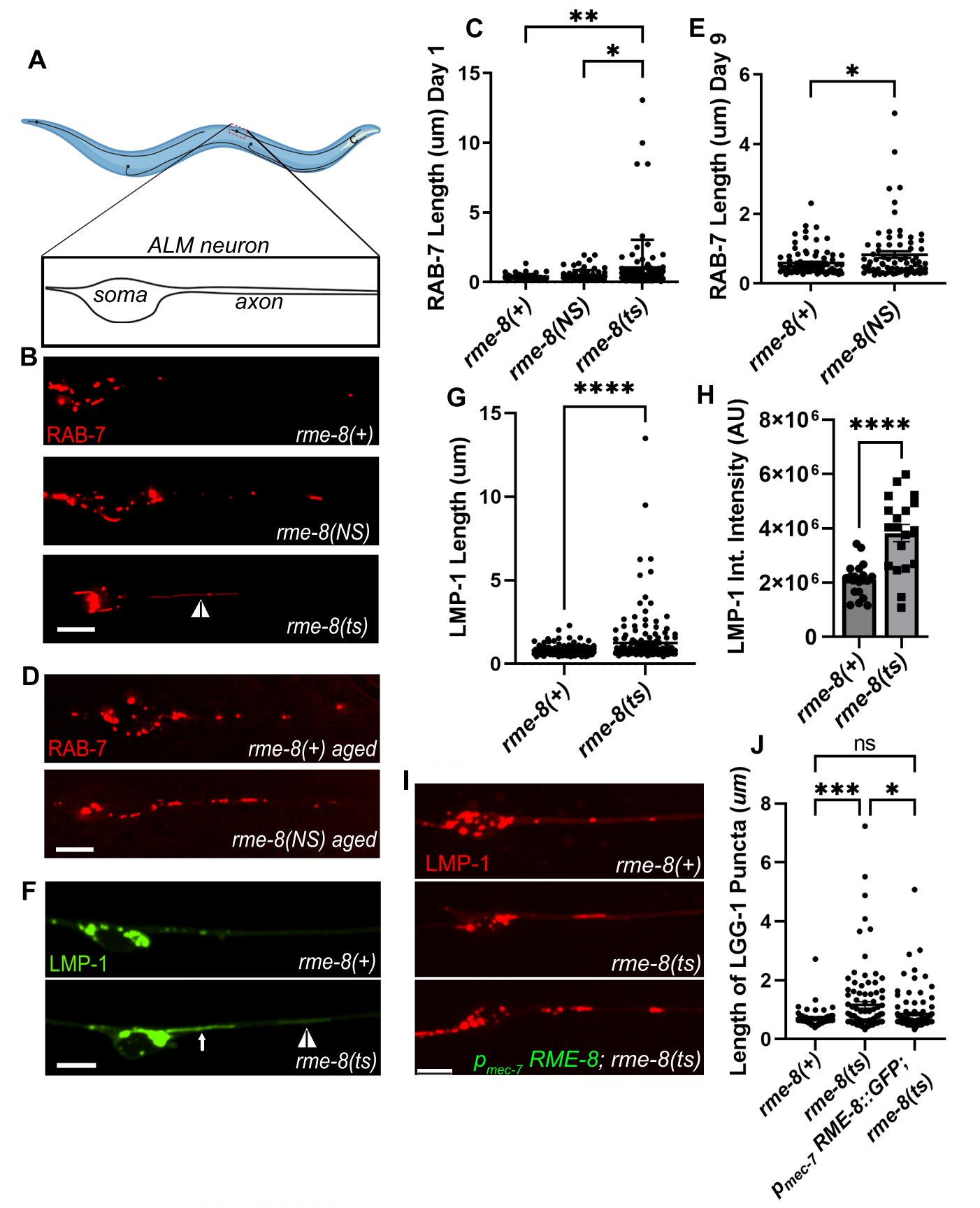
A
ALM neuron
soma
axon
B
RAB-7
rme-8(+)
rme-8(NS)
rme-8(ts)
C
RAB-7 Length (um) Day 1
**
*
rme-8(+)
rme-8(NS)
rme-8(ts)
D
RAB-7
rme-8(+) aged
rme-8(NS) aged
E
RAB-7 Length (um) Day 9
*
rme-8(+)
rme-8(NS)
F
LMP-1
rme-8(+)
rme-8(ts)
G
LMP-1 Length (um)
****
rme-8(+)
rme-8(ts)
H
LMP-1 Int. Intensity (AU)
8×10⁶
6×10⁶
4×10⁶
2×10⁶
****
rme-8(+)
rme-8(ts)
I
LMP-1
rme-8(+)
rme-8(ts)
p mec-7 RME-8; rme-8(ts)
J
Length of LGG-1 Puncta (um)
ns
***
*
rme-8(+)
rme-8(ts)
p mec-7 RME-8::GFP; rme-8(ts)

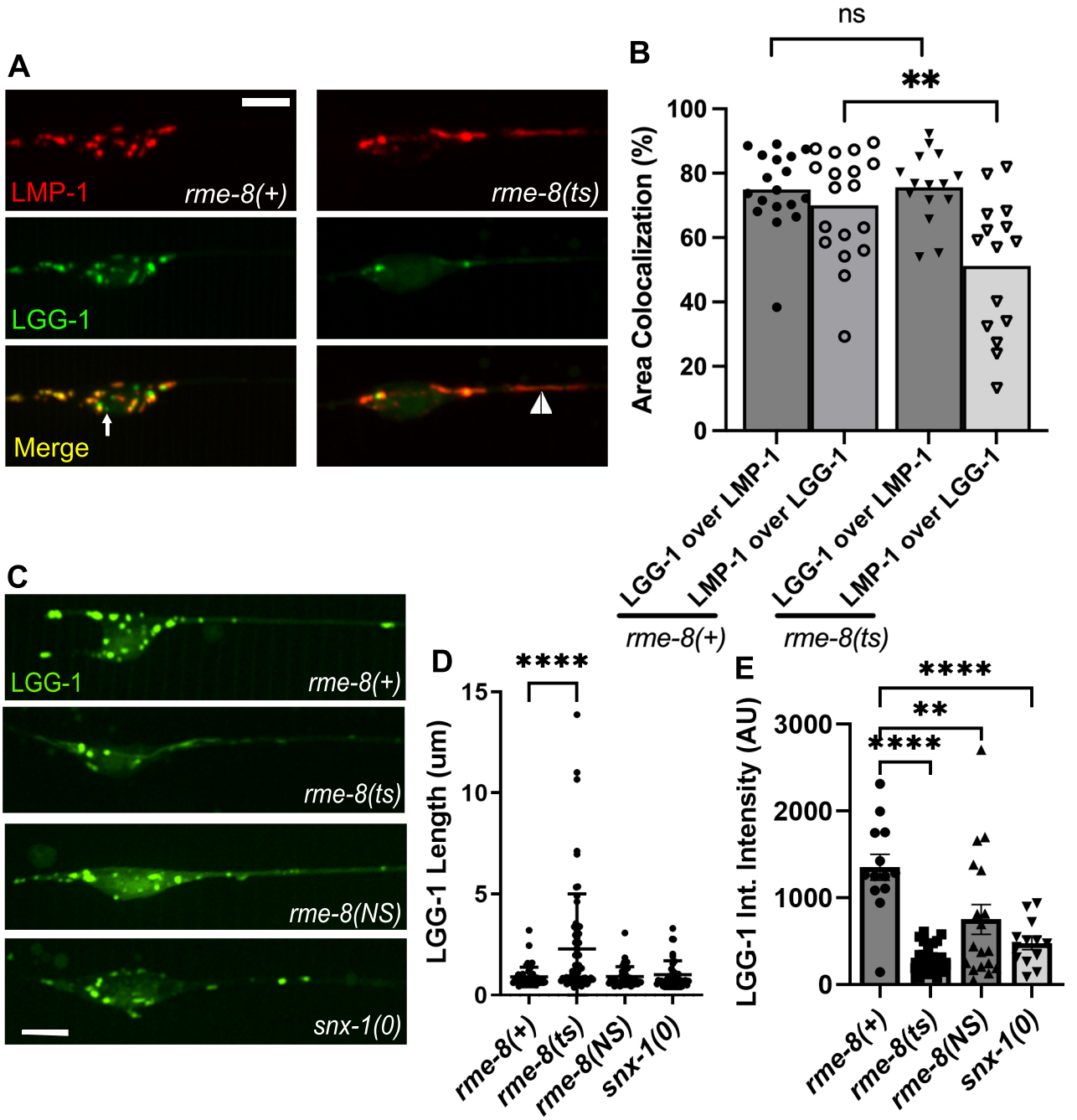
A
LMP-1
rme-8(+)
rme-8(ts)
LGG-1
Merge
B
ns
**
Area Colocalization (%)
100
80
60
40
20
0
LGG-1 over LMP-1
LMP-1 over LGG-1
LGG-1 over LMP-1
LMP-1 over LGG-1
rme-8(+)
rme-8(ts)
C
LGG-1
rme-8(+)
rme-8(ts)
rme-8(NS)
snx-1(0)
D
****
LGG-1 Length (um)
15
10
5
0
rme-8(+)
rme-8(ts)
rme-8(NS)
snx-1(0)
E
****
**
****
LGG-1 Int. Intensity (AU)
3000
2000
1000
0
rme-8(+)
rme-8(ts)
rme-8(NS)
snx-1(0)

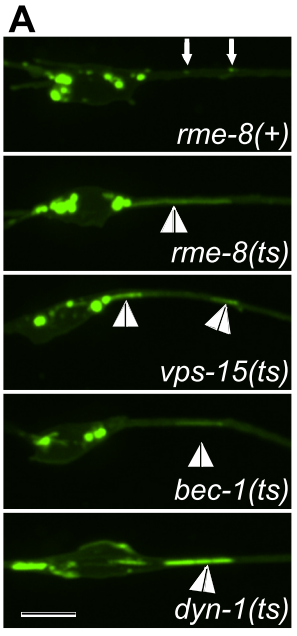
A
rme-8(+)
rme-8(ts)
vps-15(ts)
bec-1(ts)
dyn-1(ts)

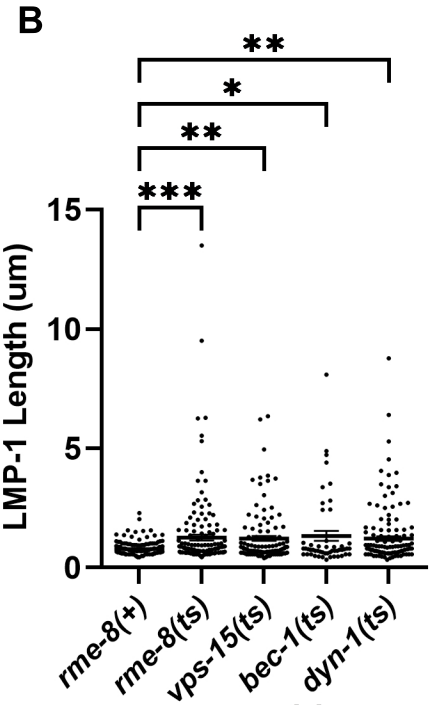
B
**
*
**
***
LMP-1 Length (um)
15
10
5
0
rme-8(+)
rme-8(ts)
vps-15(ts)
bec-1(ts)
dyn-1(ts)

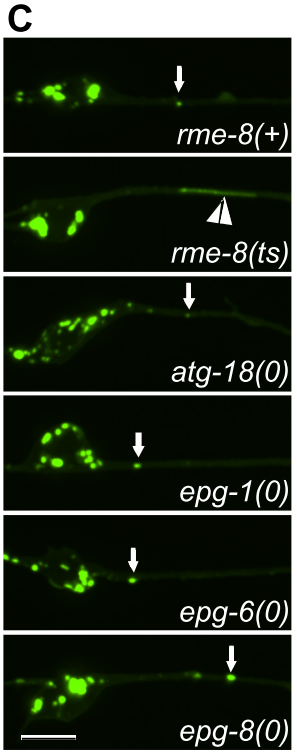
C
rme-8(+)
rme-8(ts)
atg-18(0)
epg-1(0)
epg-6(0)
epg-8(0)

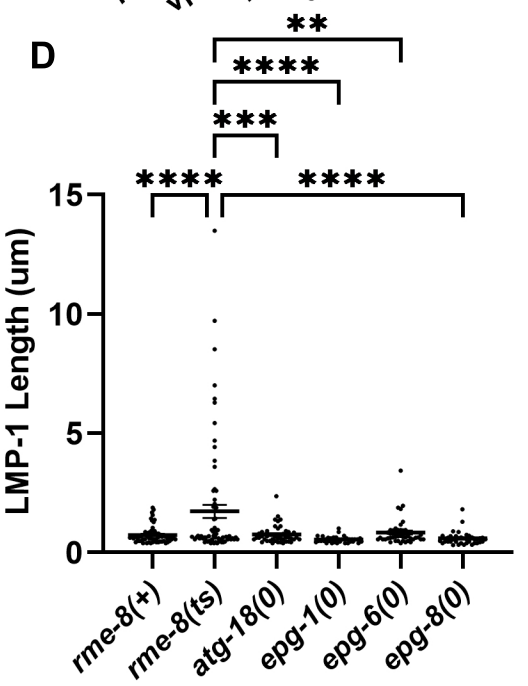
D
**
****
***
****
****
LMP-1 Length (um)
15
10
5
0
rme-8(+)
rme-8(ts)
atg-18(0)
epg-1(0)
epg-6(0)
epg-8(0)

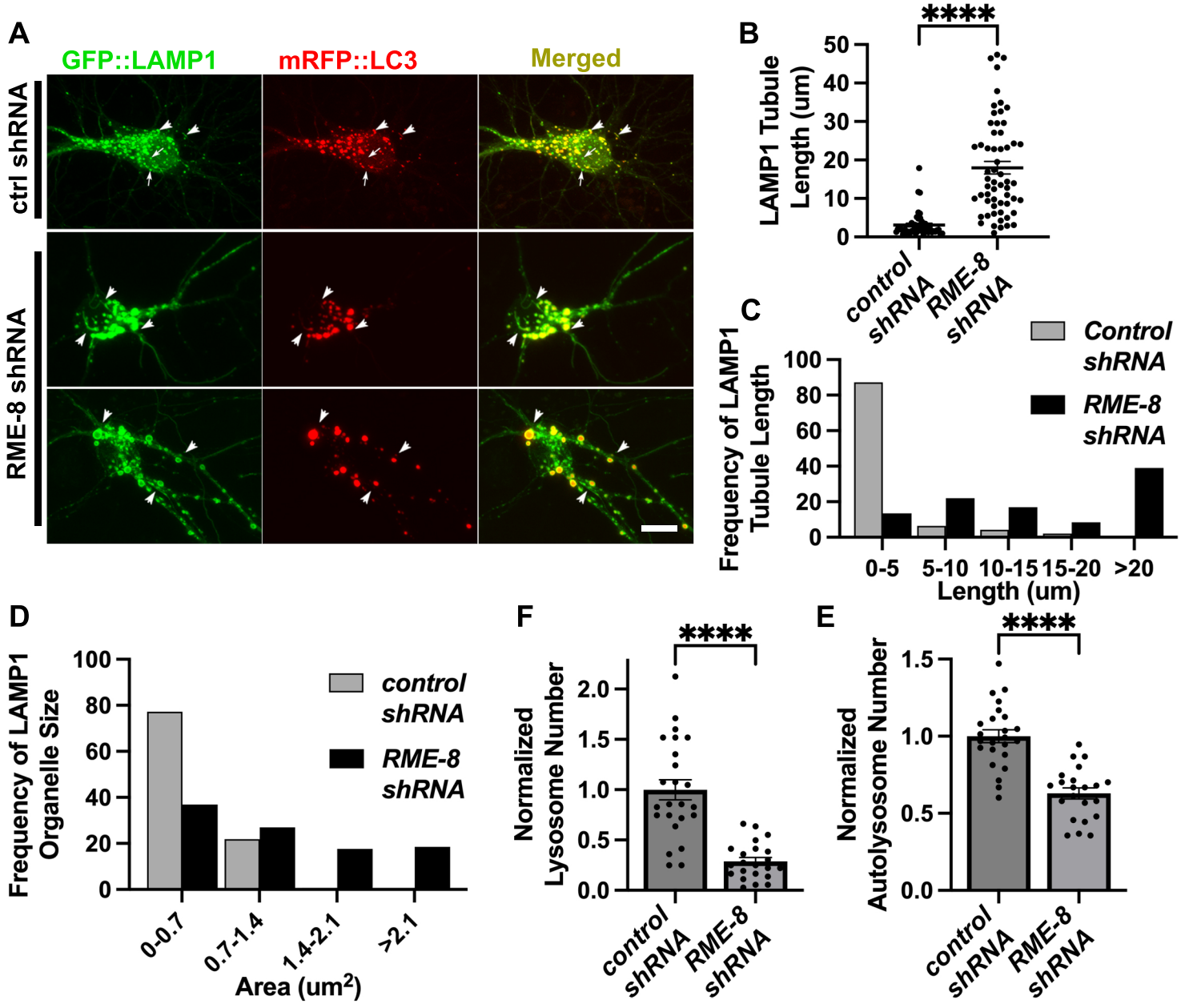
A
GFP::LAMP1
mRFP::LC3
Merged
ctrl shRNA
RME-8 shRNA
B
****
LAMP1 Tubule Length (um)
50
40
30
20
10
0
control shRNA
RME-8 shRNA
C
Frequency of LAMP1 Tubule Length
100
80
60
40
20
0
Control shRNA
RME-8 shRNA
0-5
5-10
10-15
15-20
>20
Length (um)
D
Frequency of LAMP1 Organelle Size
100
80
60
40
20
0
control shRNA
RME-8 shRNA
0-0.7
0.7-1.4
1.4-2.1
>2.1
Area (um2)
F
****
Normalized Lysosome Number
2.0
1.5
1.0
0.5
0.0
control shRNA
RME-8 shRNA
E
****
Normalized Autolysosome Number
1.5
1.0
0.5
0.0
control shRNA
RME-8 shRNA

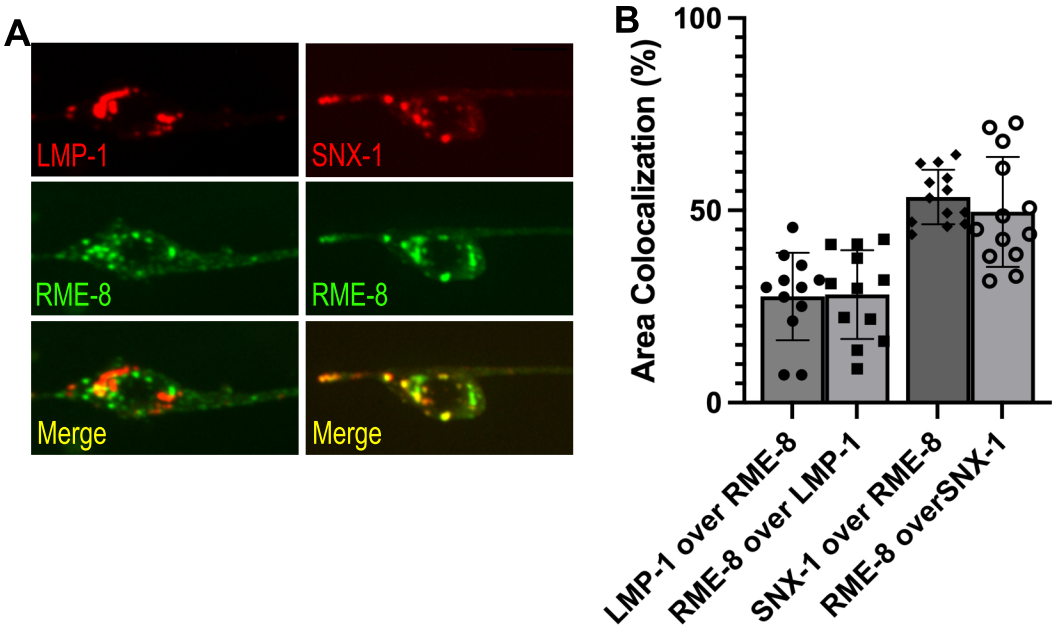
A
LMP-1
SNX-1
RME-8
RME-8
Merge
Merge
B
Area Colocalization (%)
100
50
0
LMP-1 over RME-8
RME-8 over LMP-1
SNX-1 over RME-8
RME-8 overSNX-1

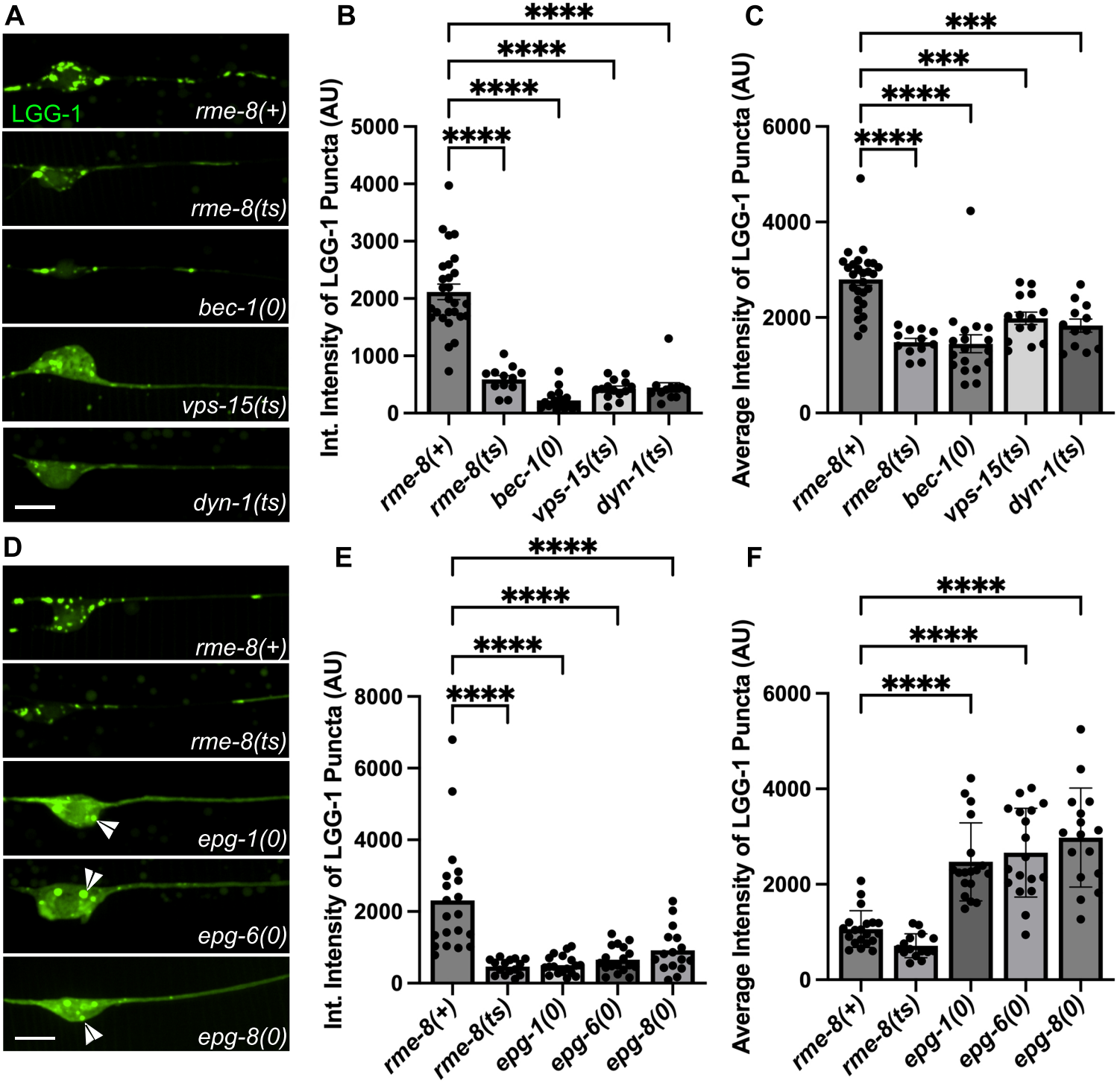
A
LGG-1
rme-8(+)
rme-8(ts)
bec-1(0)
vps-15(ts)
dyn-1(ts)
B
Int. Intensity of LGG-1 Puncta (AU)
5000
4000
3000
2000
1000
0
****
****
****
****
rme-8(+)
rme-8(ts)
bec-1(0)
vps-15(ts)
dyn-1(ts)
C
Average Intensity of LGG-1 Puncta (AU)
6000
4000
2000
0
***
***
****
****
rme-8(+)
rme-8(ts)
bec-1(0)
vps-15(ts)
dyn-1(ts)
D
rme-8(+)
rme-8(ts)
epg-1(0)
epg-6(0)
epg-8(0)
E
Int. Intensity of LGG-1 Puncta (AU)
8000
6000
4000
2000
0
****
****
****
****
rme-8(+)
rme-8(ts)
epg-1(0)
epg-6(0)
epg-8(0)
F
Average Intensity of LGG-1 Puncta (AU)
6000
4000
2000
0
****
****
****
rme-8(+)
rme-8(ts)
epg-1(0)
epg-6(0)
epg-8(0)

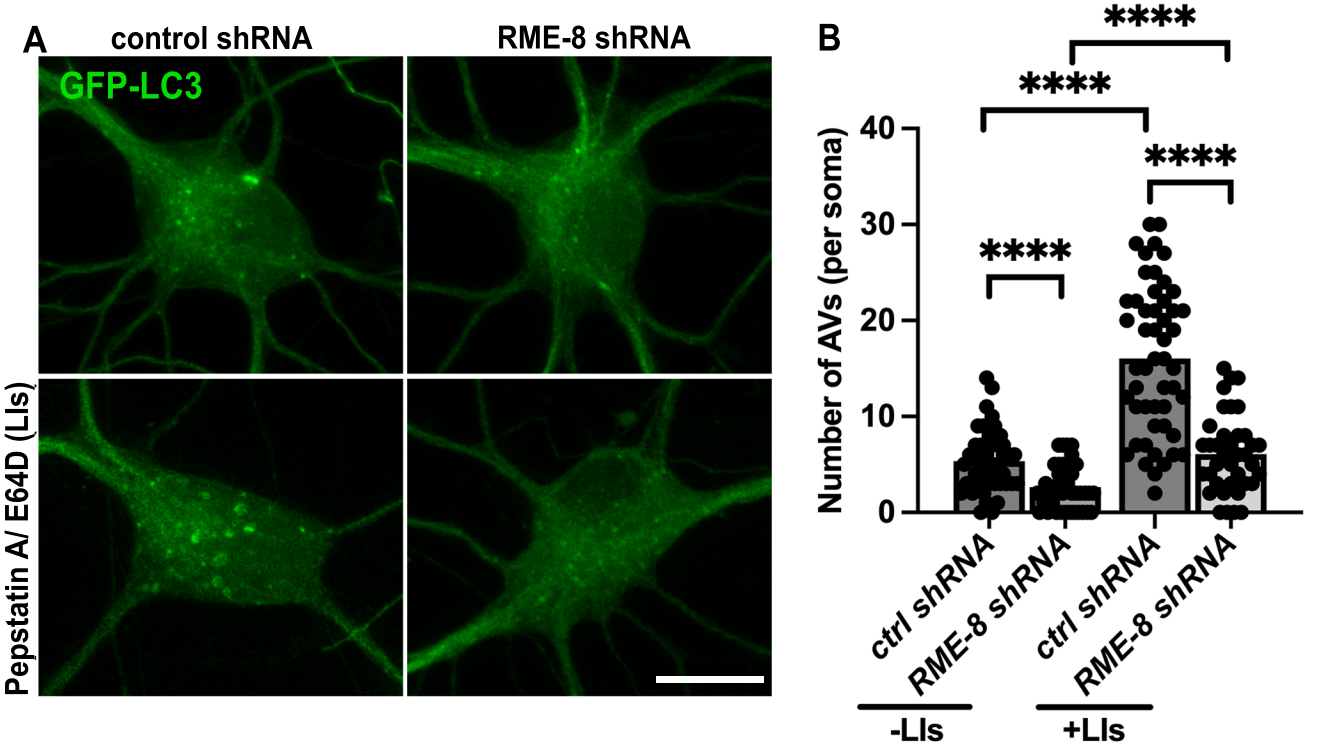
A
control shRNA
RME-8 shRNA
GFP-LC3
Pepstatin A/ E64D (LIs)
B
Number of AVs (per soma)
40
30
20
10
0
****
****
****
****
ctrl shRNA
RME-8 shRNA
ctrl shRNA
RME-8 shRNA
-LIs
+LIs

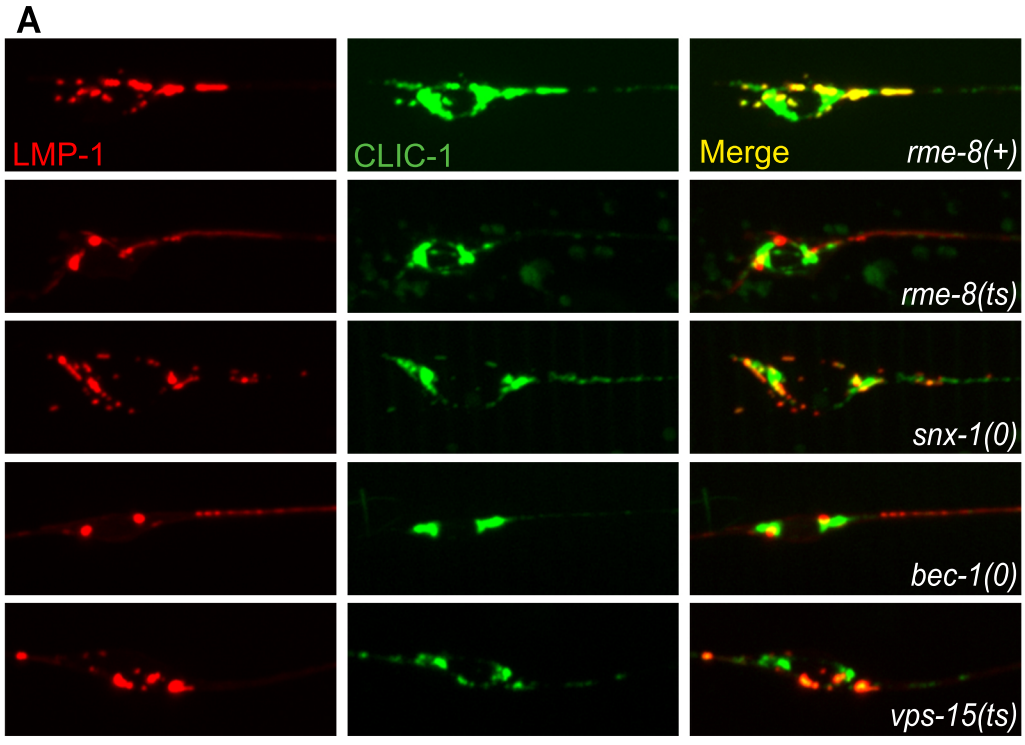
A
LMP-1
CLIC-1
Merge
rme-8(+)
rme-8(ts)
snx-1(0)
bec-1(0)
vps-15(ts)

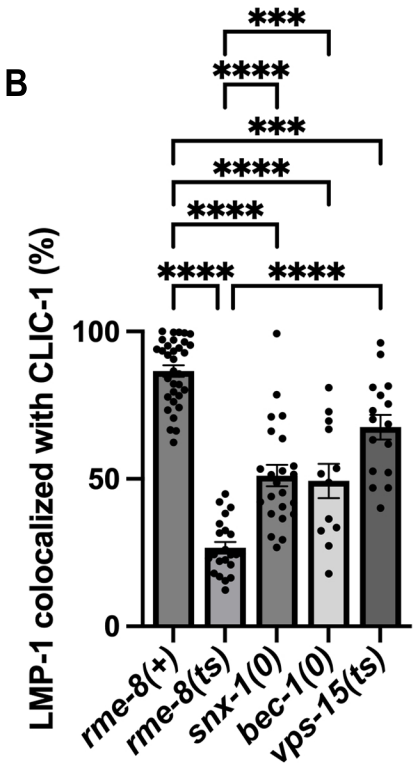
B
LMP-1 colocalized with CLIC-1 (%)
100
50
0
***
****
***
****
****
****
****
rme-8(+)
rme-8(ts)
snx-1(0)
bec-1(0)
vps-15(ts)

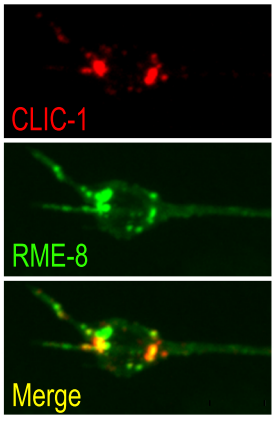
C
CLIC-1
RME-8
Merge

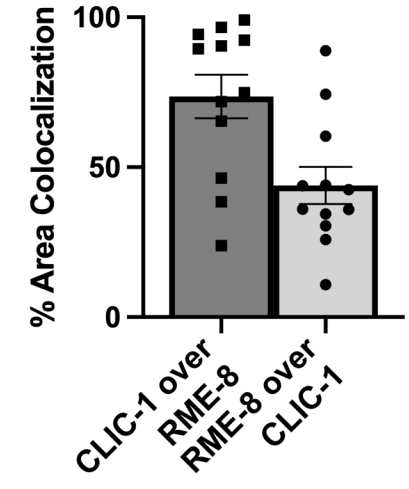
D
% Area Colocalization
100
50
0
CLIC-1 over RME-8
RME-8 over CLIC-1